SYNTHESIS OF FERRIC-POLYMER NANOCOMPOSITE FOR THE REMOVAL OF CADMIUM FROM SIMULATED WASTEWATER

A Thesis

Submitted to the College of Engineering of
Al-Nahrain University in Partial Fulfilment
of the Requirements for the Degree of Master of Science

in

Chemical Engineering

by

Zahra Aamer Ismail

(B.Sc. in Chemical Engineering, 2020)

Supervised by

Asst. Prof. Dr. Usama Akram Saed

Jamadi Al-awal   1445

November   2023

Supervisor Certification

I certify that this thesis entitled "**Synthesis of Ferric-Polymer Nanocomposite for The Removal of Cadmium from Simulated Wastewater**" was prepared under my supervision at College of Engineering/Al-Nahrain University in partial fulfilment of the requirements for the degree of **Master of Science in Chemical Engineering.**

Asst. Prof. Dr. Usama Akram Saed

Supervisor

29 / 11 /2023

In view of available recommendation, I forward this thesis for debate by

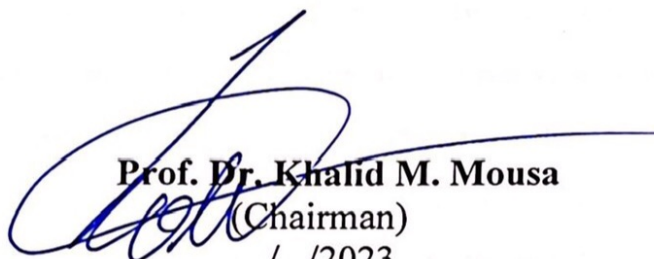**Examining committee.**

Asst. Prof. Dr. Abbas Abdulkareem Mahmood
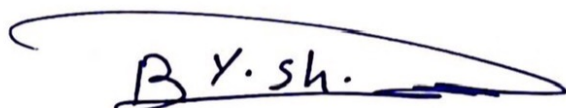
Head of Chemical Engineering Department

29 / 11 / 2023

Committee Certificate

We certify, as an Examining Committee, that we have read this thesis entitled **"Synthesis of Ferric-Polymer Nanocomposite for The Removal of Cadmium from Simulated Wastewater"** and examined the student **Zahra Aamer Ismail** in its content and what related to it, and found it adequate for the standard of a thesis for the degree of **Master of Science in Chemical Engineering.**

Prof. Dr. Khalid M. Mousa
(Chairman)
/ /2023

Asst. Prof. Dr. Bashir Y. Sherhan
(Member)
/ /2023

Dr. Mohammed S. Mohammed
(Member)
29 / 4/2023

Dr. Usama A. Saed
Asst. Prof. Dr. Usama A. Saed
(Supervisor and member)
24/ 11/2023

Approval of the College of Engineering/ Al-Nahrain University.

Prof. Dr. Jumaa Salman Chiad
Dean of the College of Engineering
30 / 1 /2023

ABSTRACT

Water contamination resulting from heavy metal presence is a significant concern that has captured the attention of researchers due to its adverse impacts on both human well-being and the environment. Regrettably, nearly 20 metals, cadmium included, resist elimination or reduction without undergoing physical or biological treatment. In response to this challenge, the technique of adsorption has emerged as a promising avenue for extracting heavy metals from polluted water. Within this specific investigation, two magnetic nanocomposites, $Fe_3O_4@SiO_2$/Poly(AANa-co-PABA) and $Fe_3O_4@SiO_2$/Poly(AANa-co-AM), were synthesized using co-precipitation methods. The two catalyst composites are characterized using XRD, FE-SEM, EDX, FTIR, AFM, TEM, and BET surface area characterization were meticulously employed to scrutinize the structural and morphological attributes of these polymers. The characterization analysis revealed the successful formation of a crystal nanostructure, confirming the chemical integration of copolymers into the magnetic silicate core-shell nanoparticle. For both P1 and P2, the average sizes were determined to be 29.13 nm and 14.66 nm, respectively. Furthermore, the surface area measurements indicated values of 37.7 m²/g for P1 and 51.3 m²/g for P2. These results highlight the controlled synthesis and distinct properties of the developed materials.

Batch adsorption process was comprehensively examined, encompassing four independent variables: duration spanning 5 to 405 minutes, solution pH ranging from 2.5 to 12, mass of catalyst varying between 0.05 to 0.3 g, and Cd(II) ion concentration spanning 25 to 150 ppm at ambient temperature. The experimental outcomes pinpointed the optimal conditions

for effective cadmium removal via the adsorption process utilizing P1 and P2 as adsorbents: neutral pH, 0.3 g adsorbent mass, 405 minutes contact time, and an initial Cd(II) ion concentration of 25 mg/L. The laboratory-scale fixed-bed column showed the breakthrough curves are flow rate independent achieving metal removal of 99 % for 405 min, at pH 8.0, influent ion concentration of 100 ppm, flow rate of 5 mL/min, and 1 cm bed height. Moreover, the Langmuir, Freundlich, and Tamkin Isotherm models were harnessed to decipher and characterize the adsorption process. Results revealed that the Freundlich model proved to be the most suitable for fitting equilibrium data (R^2= 0.98), indicating non-ideal, multi-layered adsorption where new adsorbate molecules attach to previously adsorbed ones. Conversely, P2 adhered to the Langmuir model (R^2= 0.96), suggesting monolayer adsorption on a homogenous adsorbent surface with no intermolecular interactions. In the realm of kinetics, the study demonstrated that the experimental data for both nanocomposites aligned well with the pseudo-second-order model with almost perfect correlation coefficient of 0.99 and 0.99 respectively, surpassing other kinetic models in accuracy.

List of Contents

Contents   Page

Notations

Symbols		Notations
C_e	=	Equilibrium concentration
C_o	=	Initial concentration before adsorption
k_1	=	The first-order rate constant
k_2	=	The second-order rate constant
m	=	Mass of adsorbent
q_e	=	Equilibrium adsorption capacity
$R\%$	=	Removal efficiency

Abbreviation

AANa	=	Sodium acrylate
AM	=	Acrylamide
MNPs	=	Magnetic nanoparticles
NPs	=	Nanoparticles
P1	=	$Fe_3O_4@SiO_2$/Poly(AANa-co-PABA)
P2	=	$Fe_3O_4@SiO_2$/Poly(AANa-co-AM)
PABA	=	4-Aminobenzoic acid
WHO	=	World Health Organization

List of Tables

List of Figures

CHAPTER 1

INTRODUCTION

1.1 Background

Due to their capacity for accumulation and persistent existence, heavy metals are considered predominant pollutants among the diverse array of toxic substances released into water due to human activities. These metals, characterized by their high density and toxicity, pose a significant threat to the environment and living organisms. Anthropogenic sources, including industrial activities, mining, agriculture, and improper waste disposal, contribute to the introduction of heavy metals into aquatic life **(Shrestha et al., 2021).** Their long-term presence in the environment further exacerbates the risks they pose, as they can persist and continue to exert harmful effects even after the initial contamination event. Therefore, addressing the issue of heavy metal pollution is of utmost importance for the preservation of water quality and the protection of both aquatic life and human health **(Wang et al., 2020)**. While iron (Fe), copper (Cu), manganese (Mn), and zinc (Zn) are crucial for the functioning of living organisms at specific levels, the risk of toxicity arises as their concentrations escalate. Consuming drinking water that contains substantial quantities of these metals can lead to detrimental health consequences ranging from breathing difficulties to various forms of cancer **(Saha *et al.*, 2017)**. In contrast, certain metals such as arsenic, mercury, cadmium, and lead exhibit high toxicity even at minimal levels, without any recognized advantages for human well-being **(Motitswe, Badmus and Khotseng, 2022)**.

The absence of any advantageous functions for higher organisms, combined with its classification as one of the most toxic metal ions, renders cadmium a significant global environmental concern **(Christy *et al.*, 2023)**. The contamination of the environment with cadmium poses a serious problem for both humans and the ecosystem. Various industrial activities like ceramics, metal plating, and textile production release cadmium into the environment **(Saha *et al.*, 2016)**. Numerous techniques have been devised for eliminating heavy metal ions from water, such as membrane technology, ion exchange, phytoremediation, and adsorption. On the other hand, the adsorption technique presents several benefits for treating low-concentration wastewater. It stands out for its economical nature, impressive adsorption capabilities, fast rate of adsorption, absence of sludge generation, energy efficiency, and straightforward operation **(Da'na and Sayari, 2012).**

In recent years, there has been an increasing interest in utilizing magnetic nanoparticles (MNPs), specifically Fe_3O_4, as adsorbents for eliminating heavy metal ions from aqueous solutions. This is primarily attributed to their substantial surface area and distinctive super paramagnetism **(Lunge, Singh and Sinha, 2014)**. However, Fe_3O_4 MNPs encounter significant challenges, such as vulnerability to oxidation and aggregation, which can restrict their surface area, impede recyclability, and diminish their reactivity **(Boruah *et al.*, 2015)**. To overcome these challenges, a protective coating layer is often applied to enhance chemical stability and dispersibility **(Boruah *et al.*, 2015)**. Silica has been widely recognized as an excellent coating material for Fe_3O_4 MNPs due to its biocompatibility, chemical stability, and ease of surface modification.

Earlier research has provided evidence of the efficacy of $Fe_3O_4@SiO_2$ magnetic composite particles in the adsorption process, displaying notable attributes of rapidity and robust adsorption capabilities **(Fan *et al.*, 2012)**.

Additionally, polymers containing polycarboxyl and polyamino groups have exhibited exceptional abilities in adsorbing heavy-metal ions. These findings that the potential of $Fe_3O_4@SiO_2$ composite particles and specific polymer-based adsorbents in effectively capturing and removing heavy-metal ions, showcasing their promising applications in the field of adsorption technologies **(Song *et al.*, 2019)**.

1.2   The Objectives of The Study

The goal of this work is to estimate the adsorption capability of numerous developing nano adsorbents that may be obtained by:

1. Preparation and characterization of magnetic oxide Fe_3O_4 by the chemical co-precipitation method and coated with silica to become $Fe_3O_4@SiO_2$, then various polymers are loaded to increase the efficiency of the catalyst.

2. Eexamine the physical and chemical properties of the synthesized adsorbents.

3. Adsorption experiments, investigate the adsorption efficiency of the produced nanocomposites in removing cadmium (II) from stock solution using batch and continuous.

4. Employ various models to analyse adsorption isotherms and kinetics for a comprehensive understanding of the process.

CHAPTER 2

LITERATURE SURVEY

2.1 Introduction

In this chapter, the focus is on addressing the issue of water contamination caused by heavy metals. It explores various treatments commonly employed to tackle this problem, with a particular emphasis on the adsorption technique. This chapter delves into the different varieties of adsorption techniques, the factors that influence their effectiveness, as well as the various types of nanomaterials used in this context. Lastly, it provides a concise summary of previous research conducted in this field.

2.2 Water Contamination.

Water pollution is a growing problem that affects the quality of our water sources. Human activities such as industrial discharge, sewage treatment, chemicals, papers, petroleum, and metal mining processes are among the leading causes of water pollution. Contaminated water can have devastating effects on the environment, as well as on human health. It can harm aquatic life, reduce biodiversity, and even render water sources unusable for drinking, irrigation, and recreation. In order to stop water contamination, it is crucial for individuals and communities to take action and adopt more sustainable practices **(Sharma and Bhattacharya, 2017)**.

2.3   Heavy Metal Ions

Heavy metals encompass a collection of metallic elements recognized for their elevated density and harmful effects on living organisms. Among the frequently recognized heavy metals are lead, mercury, cadmium, and chromium. Prolonged contact with these heavy metals can present a substantial threat to health, particularly if they amass within the body. This accumulation has the potential to disrupt cellular functions and inflict harm upon on crucial organs. The effluents generated by various industries cause multiple environmental damages and affect humans as well as the environment. Heavy metal contamination of wastewater and effective treatment is one of the world's greatest challenges **(Ali and Khan, 2018)**.

Although heavy metals can play essential roles in biological systems when present in trace amounts. However, their significance lies in their potential toxicity when they accumulate in significant quantities. These elements persist in the environment because they are not easily broken down through natural processes. The movement of heavy metals within ecosystems, spreading through the air, water, and soil, is primarily driven by human activities **(Thilagan *et al.*, 2015)**.

2.3.1 Cadmium Ions: Sources and Toxicity Effects

Cadmium, a highly toxic element, poses a significant threat to living organisms, even when present in low concentrations. Its detrimental effects on various biological systems are well established. In industrial contexts, cadmium is frequently found in association with zinc and copper minerals, as it often occurs as an impurity or contaminant in the ore deposits of these metals. Consequently, it becomes a byproduct of the mining, smelting, and refining processes involved in zinc and copper production **(Liu *et al.*, 2020)**.

Naturally, Cadmium exists in the environment as a result of the progressive erosion and abrasion of rocks and soils, as well as through unique events such as volcanic activity and forest fires. As a result, it is naturally present in the air, water, soil, and food **(Liu *et al.*, 2020)**.

Cadmium poisoning first gained attention with the infamous itai-itai disease **(Aoshima, 2016)** in the sixties of the last century in Japan, which was caused by the intake of cadmium-contaminated rice. Cadmium possesses a lengthy biological half-life of 20 years and primarily impacts the liver, kidneys, and intestine. Knowing that the permissible limits for the intake of cadmium ions is equivalent to 0.025 (mg/L), prolonged exposure to cadmium has demonstrated a correlation with cancer development in various systems, including the liver, kidney, lung, prostate, hematological, and others. This establishes cadmium as a recognized carcinogen. Overall, cadmium induces the generation of stress proteins. The outcome in animal cells, which could involve apoptosis, growth inhibition, proliferation, or carcinogenic effects, depends on factors like exposure quantity, duration, cell type, and the presence of other chemical compounds **(Sarkar, Ravindran and Krishnamurthy, 2013)**.

Other metals, their source, toxicity effect, and permissible limit in (mg/l) of each metal according to World Health Organizations (WHO) for the human body are summarized in Table 2-1.

Table 2-1: Source, toxicity effect and permissible limit for the heavy metals

Metal & (Ref.)	Sources	Toxicity	Permissible limit(mg/L)
Mercury (Hg) **(Khulbe and Matsuura, 2018)**	Mercury contamination arises from both natural sources, including volcanic activity and geological processes, and human-made sources such as pharmaceutical and cosmetic production, paper and pulp industries, batteries, and medical drugs	It causes neurological damage, paralysis, blindness, rheumatoid arthritis and anorexia	0.001
Lead (Pb) **(Veerakumar *et al.*, 2015)**	Lead contamination can be found in the water streams of various industries, including those involved in battery manufacturing, ammunition production, bronze items and piping, as well as ceramic and glass manufacturing.	Brain damage, anemia, anorexia, vomiting, and disease of circulatory and nervous systems	0.05
Chromium (Cr) **(Georgieva *et al.*, 2015)**	The origins of chromium contamination in water streams encompass steel fabrication, paint and pigment production, chemical industries, textile manufacturing, ceramics, and units involved in wood treatments.	It causes cancer in the digestive tract, headache, nausea, vomiting, lung tumor, and hemorrhage	0.05
Nickel (Ni) **(Guarín-Romero *et al.*, 2019)**	Chemical industries, electroplating operations, mining, and refining activities, as well as units engaged in paint and ink formulation.	Dermatitis, nausea, chronic asthma, coughing and cancer	2.0

Zinc (Zn) **(Sen and Khoo, 2013)**	Numerous industrial activities such as mining, galvanization, stabilizers, steel production, burning of coal, and purification of zinc	Depression, lethargy, neurological signs, and increased thirst and loss of appetite	5.0
Copper (Cu) **(Danesh, Ghorbani and Marjani, 2021)**	Paints and pigments, tanneries, fertilizers and cleaning and plating baths, etc.	Wilson disease, liver damage, insomnia, renal damage, nausea, and lung cancer.	2.5
Arsenic (As) **(Alka *et al.*, 2021)**	Various sources, such as insecticides, herbicides, phosphate fertilizers, mining, semi-conductor industries, coal combustion	Arsenicosis, skin, lung, bladder and kidney cancer, neurological disorder, muscular weakness, and nausea	0.01
Cadmium(Cd) **(Sarkar, Ravindran and Krishnamurt hy, 2013)**	Mining, smelting, and manufacturing of batteries, industrial processes.	Kidney disease, neurotoxicity, cardiovascular effects	0.025

2.4   Conventional Heavy Metal Ions Removal Techniques

Ion exchange, chemical precipitation, coagulation, membrane separation, electro-coagulation, and reverse osmosis are all techniques for eliminating heavy metal ions.

2.4.1 Ion Exchange

Over the past few decades, the technique of ion exchange has found significant application in purifying water by eliminating impurities. This process involves a combination of physical and chemical actions wherein cations present in wastewater are substituted with metal ions through the utilization of ion exchange methods. Within this procedure, both synthetic resins and naturally occurring zeolites are employed. Zeolites, in particular, are widely favoured due to their distinctive capability to selectively extract various metals **(Okamoto and Takahashi, 2020)**.

2.4.2   Chemical Precipitation

Due to its user-friendly nature and economical advantages, chemical precipitation stands as a commonly employed conventional method for eradicating heavy metal ions from contaminated water. This time-honored process involves the interaction of chemical agents with metal ions to create precipitates of low solubility, a step that can be followed by filtration to isolate these substances. The induction of metal precipitation is executed through the introduction of chemical reactants like alum, lime, and limestone. However, chemical precipitation is burdened by notable downsides, including the excessive consumption of chemical agents during heavy metal treatment, the generation of substantial quantities of sludge, and the significant expenses associated with sludge disposal **(Sun et al., 2020).**

2.4.3 Membrane Separation

Based on the size of the particle, different types of membranes, including ultrafiltration, nanofiltration, and electrodialysis, are employed in the membrane separation process to remove heavy metal ions from wastewater. The benefits of these technologies include using fewer chemicals and producing less sludge, but the process is hindered by high maintenance and operating costs **(Hussain, Madan and Madan, 2021)**.

2.4.4 Reverse Osmosis

A semi-permeable membrane is employed in reverse osmosis to separate heavy metal ions from an aqueous solution. Purified water flows into the dilute side of the membrane when pressure is applied from the concentrated side, and pollutants from the high concentration side may be removed with water from the dilute side. This technique may be used to remove various industrial effluents from the pulp and paper, textile, tannery, and electroplating sectors. It has a few drawbacks, including high chemical costs and high power requirements for pumping pressure **(Wang and Guo, 2020)**.

2.4.5 Coagulation

Coagulation is a water treatment method characterized by the utilization of chemicals to eliminate contaminants from water sources. Within the coagulation procedure, a specific chemical compound known as a coagulant, which could be aluminium sulfate or ferric chloride, is introduced into the water. This coagulant prompt small particles present in the water to aggregate and assemble into larger clusters, referred to as flocs. After this aggregation, the flocs are separated from the water through sedimentation or

filtration mechanisms. Nevertheless, this technique has its drawbacks, notably the necessity for costly reagents and the generation of an excessive amount of sludge, accompanied by the challenge of disposing of this hazardous sludge safely within the environment **(Shrestha et al., 2021)**.

2.4.6 Adsorption

The accumulation of atoms or molecules of a fluid (adsorbate) on the surface of a solid (adsorbent) is known as adsorption . This process results in the formation of a dense layer of particles or atoms on the surface of the adsorbents. Adsorption is a phenomenon that takes place in the vast majority of natural physical, biological, and chemical systems. It finds extensive use in industrial contexts, including applications like activated charcoal, synthetic resins, and water filtration. Presently, adsorption is seen as the most optimal strategy for treating wastewater, primarily due to its straightforward nature and its ability to offer cost-effective solutions. Adsorption is a typical approach for removing metal ions from various industrial effluents **(Yao et al., 2022) (Wang et al., 2023)**.

A class of adsorbents currently receiving growing attention is the polymers nanocomposite adsorbents. it is effectively treating water by adsorption. When compared to other adsorbents, they have a greater adsorption capacity and longer life cycles. As a result, they have a great deal of potential as extremely effective water and waste treatment agents **(Mukhopadhyay et al., 2020)**.

These adsorbents have a fundamental physicochemical feature, such as internal surface area and pore size distribution, may be changed by adjusting the polymerization conditions. In comparison to activated carbon, exhausted

polymeric adsorbents may be efficiently regenerated under moderate conditions such as acid or alkaline washing **(Wolska et al., 2023)**.

The excellent properties of polymers compared to traditional adsorbents make their use in the treatment of contaminated waters very promising. This has the potential to lower costs and generate less contamination. **(Tao et al., 2020)**. Traditional polymeric adsorbents were developed during the 1960s **(Tian *et al.*, 2023)** for use in gel permeation chromatography, but their remarkable physical qualities have made them a highly popular material for adsorption and filtering operations. They are now often employed to remove organic contaminants from industrial wastewaters or fresh water **(Singh *et al.*, 2023)**.

2.4.6.1   Types of Adsorption

There are two types of adsorption mechanism physisorption and chemisorption, physisorption and chemisorption are two distinct adsorption processes that differ in their mechanisms, bond strength, reversibility, temperature dependence, selectivity, and applications **(Sharma et al., 2023)**. The Comparison between them are listed in the Table 2-2.

Table 2-2: Comparison between physisorption and chemisorption.

Terms	Physisorption	Chemisorption
Mechanism of adsorption	Involves the weak van der Waals forces between the adsorbate and the adsorbent	Involves the formation of strong chemical bonds.
Reversibility	Reversible	Irreversible
No. of layers	Multi-layer	Monolayer
Adsorbate types	Occurs with non-polar molecules like gases	Usually involves polar or ionic molecules
Surface area limitations	Limited by the surface area of the adsorbent	Not limited by the surface area
Adsorption energy	Lower than that of chemical adsorption	Higher than Physisorption
Effect on Adsorbate and adsorbent properties	Typically, does not change the chemical and physical properties	Can change the chemical and physical properties of both the adsorbate and the adsorbent
Bond strength	The bonds formed in physisorption are weak, with energies in the range of 1-40 kJ/mol	The bonds formed are much stronger, with energies in the range of 40-800 kJ/mol.
Heat of adsorption	About 5 kcal/mol, Exothermic	(20-100) kcal/mol, exothermic or endothermic, depends on the reaction
Applications	Often used in gas separation, purification, and storage	Used in catalysis, surface modification, and sensing applications.

2.4.6.2   Factor Effecting on The Adsorption

There are several factors affecting the adsorption process which are listed below, which are mostly impacted by the functioning of the bulk solution and the adsorbent properties utilized;

- **Contact Time:** Adsorption tends to increase with time as the adsorbate molecules come into contact with the adsorbent surface and gradually adhere to it. At the beginning of the adsorption process, the rate of adsorption may be relatively high as there are many available adsorption sites on the surface of the adsorbent. As the adsorption process continues, however, the number of available sites on the adsorbent surface may decrease, which can lead to a decrease in the rate of adsorption **(Çelebi, Gök and Gök, 2020).**

- **Adsorbent Dose:** As the dose of the adsorbent increases, the number of available adsorption sites increases, leading to an increase in the adsorption capacity of the adsorbent ,up to a certain point **(Bilal *et al.*, 2021)**.

- **pH of the Solution:** In adsorption media, pH is used to measure the concentration of hydrogen ions. While not linearly proportional, the adsorptive loading of metal cations increases with the rising pH of the adsorption structure. Very acidic and basic conditions do not produce adsorption because hydrogen protons and hydroxyl ions interact in the appropriate active pores on the adsorbent surface **(Çelebi, Gök and Gök, 2020)**.

- **Adsorbate Concentration:** At low concentrations, the adsorbate molecules have a greater chance of colliding and adhering to the adsorbent surface. As the concentration of the adsorbate increases, the number of available sites on the adsorbent surface decreases, and adsorption becomes less efficient **(Bilal *et al.*, 2021)**.

- **Particle Size and Surface Area of Adsorbent:** The optimal particle size for adsorbent depends on the specific reaction and the desired properties of the catalyst. In some cases, smaller particle sizes can be advantageous because they can increase the surface area of the catalyst, leading to higher activity and selectivity. This surface area is quantified as square meters per gram (m^2/g). However, smaller particles may also be more prone to agglomeration, deactivation, and loss of selectivity. On the other hand, larger particle sizes can be more stable and less prone to deactivation, but they may have a lower surface area, leading to lower activity and selectivity. Therefore, the best particle size for a catalyst depends on a trade-off between activity, selectivity, stability, and other factors **(Liu and Corma, 2018)(Sun, Li and Xu, 2018)**.

- **Effect of Temperature:** Adsorption is an exothermic process, meaning that it releases heat as the adsorbate molecules bind to the adsorbent surface. Therefore, at high temperatures, the adsorbate molecules may have enough energy to break the chemical bonds formed during adsorption, leading to decreased adsorption capacity **(Masulli et al., 2022)**.

- **Agitation Speed:** Agitation refers to the mixing or stirring of the solution containing the adsorbate and adsorbent, and it influences the rate at which the adsorbate molecules come into contact with the adsorbent surface. At low agitation speeds, the rate of mass transfer between the bulk solution and the adsorbent surface may be slow, resulting in a slower adsorption rate. As agitation speed increases, the rate of mass transfer also increases, leading to a faster adsorption rate. However, at very high agitation speeds, the adsorbate molecules may not have enough time to interact with the adsorbent surface, and the adsorption rate may decrease. Additionally, high agitation speeds can also lead to particle attrition or fragmentation, which can reduce the effectiveness of the adsorbent **(Dhawane, Kumar and Halder, 2016)**.

2.5   Nanomaterials Overview

Nanomaterials are materials that have at least one dimension measuring less than 100 nanometers (nm). They have unique properties and can be classified based on their composition, size, shape, and structure. Some common types of nanomaterials include **(Lu *et al.*, 2016)** :

2.5.1 Nanoparticles:

These are solid particles that range in size from 1-100 nm. They can be made of metals, semiconductors, or polymers and have applications in electronics, medicine, and energy storage.

2.5.2 Nanotubes:

These are hollow tubes with diameters of 1-100 nm and lengths up to several microns. They can be made of carbon, metal oxides, or other materials and have applications in electronics, energy storage, and drug delivery.

2.5.3 Nanowires:

These are solid wires with diameters of 1-100 nm and lengths up to several microns. They can be made of metals or semiconductors and have applications in electronics and energy storage.

2.5.4 Nanoporous Materials:

These are materials that have pores or channels at the nanoscale. They can be made of metals, ceramics, or polymers and have applications in catalysis, gas separation, and water purification.

2.5.5 Nanocomposites Materials:

These are materials that combine two or more types of nanomaterials to create a new material with unique properties. They have applications in medicine, energy storage, and environmental remediation.

2.6   Composite Materials with Nano-Scale Components

Nanocomposite materials are materials that are composed of a matrix material and one or more types of nanoscale fillers or reinforcements **(Goyal, 2017)**, Here are types of nanocomposites material Figure 2-1:

```
                    ┌──────────────────────────┐
                    │  Nanocomposites Material  │
                    └──────────────────────────┘
              ┌──────────────┴──────────────┐
              ▼                              ▼
    ┌──────────────────┐          ┌──────────────────┐
    │  Polymer based   │          │ Non polymer based│
    └──────────────────┘          └──────────────────┘
```
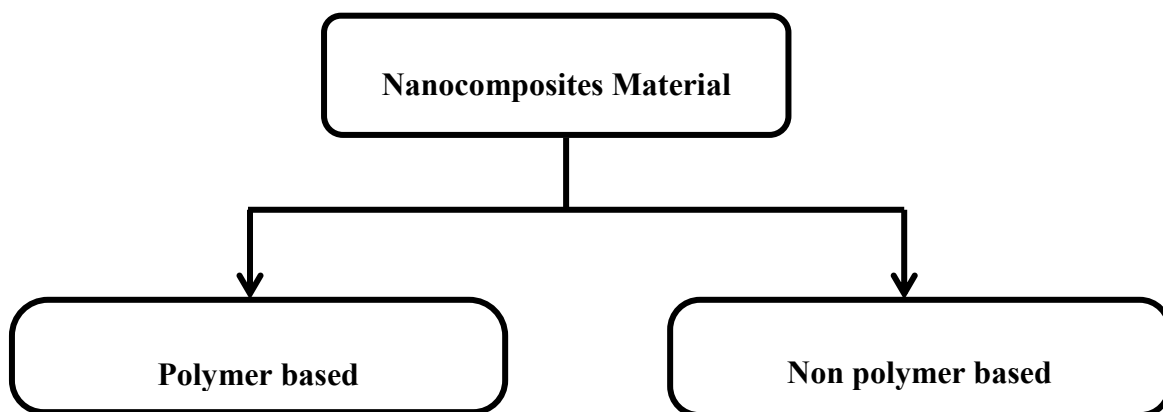
Figure 2-1: Types of nanocomposites material.

2.6.1 Polymer Based Nanocomposite:

A polymer-based nanocomposite is a type of composite material consisting of a polymer matrix reinforced with nanoparticles. The nanoparticles used in nanocomposites are typically inorganic particles, such as clay, silica, or metal oxides, with dimensions ranging from 1 to 100 nanometers. The addition of nanoparticles to the polymer matrix can

significantly enhance the mechanical, thermal, electrical, and barrier properties of the resulting nanocomposite material. This is because the high surface area of the nanoparticles and their small size allow them to disperse evenly within the polymer matrix, leading to a more homogeneous distribution of the reinforcing phase. Polymer-based nanocomposites have numerous potential applications, including in the automotive and aerospace industries, electronics, packaging, and medical devices. They are also being researched for their potential use in energy storage and conversion devices, such as batteries and solar cells. Polymer-based nanocomposite is divided into several types according to Figure 2-2 **(Goyal, 2017)**.
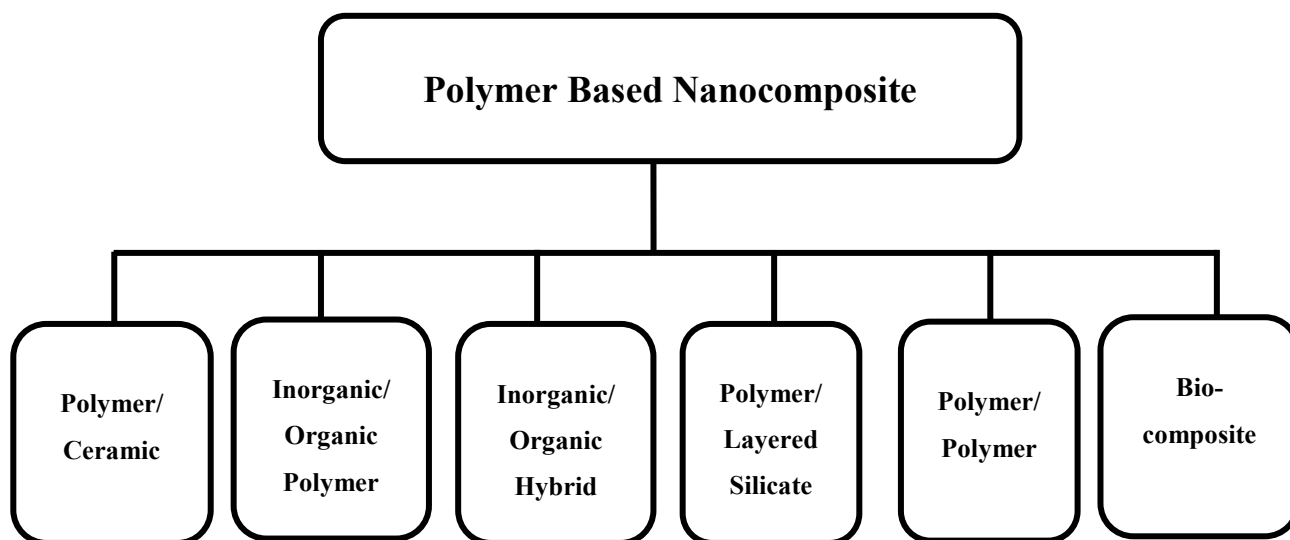
Figure 2-2 : Types of polymers based nanocomposite

2.6.1.1   Polymer/Ceramic Nanocomposite

Polymer/ceramic nanocomposites are hybrid materials formed by integrating ceramic nanoparticles into a polymer framework. These ceramic nanoparticles have the capability to enhance attributes like rigidity, resilience,

and durability, along with bolstering the thermal resilience and fire resistance of the polymer matrix **(Kumar, Supriya and Kar, 2018)**.

2.6.1.2   Inorganic/ Organic Polymer Nanocomposites

These composite materials are produced by distributing inorganic nanoparticles, organic compounds, or a blend of the two within a polymer framework. Inorganic constituents like clays or carbon nanotubes have the potential to elevate mechanical characteristics, while organic compounds such as monomers or surfactants can enhance the harmonious interaction between the inorganic constituents and the polymer matrix **(Khalid et al., 2020)**.

2.6.1.3   Inorganic/Organic Hybrid Nanocomposite

Hybrid nanocomposites combining inorganic and organic components bring forth a variety of benefits when compared to conventional standalone inorganic or organic materials. Notably, they can exhibit enhanced mechanical, thermal, and optical characteristics, along with heightened chemical stability and increased resilience against degradation **(Lu, 2020)**.

2.6.1.4   Polymer/Layered Silicate Nanocomposites

These composite materials are generated through the dispersion of small quantities of layered silicate nanoparticles within a polymer matrix. The substantial aspect ratio of these layered silicate nanoparticles, coupled with their significant surface area relative to volume, serves to augment mechanical attributes **(Koo, 2019)**.

2.6.1.5 Polymer/Polymer Nanocomposites

Nanocomposites composed of polymers, known as polymer/polymer nanocomposites, are created by merging two or more polymers at the nanoscale dimension. These composite structures can provide distinctive characteristics, including enhanced mechanical robustness, heightened thermal resilience, and superior attributes as gas barriers **(Fakirov, 2018)**.

2.6.1.6 Biocomposites

Biocomposites are composite materials made from natural fibers or biodegradable polymers combined with a matrix material, such as a synthetic polymer to form a new material with improved properties. The use of natural fibers makes biocomposites more environmentally friendly alternative to traditional composites **(Nagalakshmaiah *et al.*, 2019)**.

2.6.2 Non-Polymer Based Nanocomposite

A non-polymer based nanocomposite is a material made up of two or more substances, where one substance is a non-polymeric material and the other is nano-sized particles. These particles are added to the non-polymeric material in small amounts to improve its properties like strength, durability, and conductivity. The resulting material is stronger, lighter, and more resistant to wear and tear than the original non-polymeric material **(Goyal, 2017)**.

2.7   Adsorption Isotherms

Adsorption isotherms serve as fundamental tools employed to comprehend the behavior of adsorbents, which are substances utilized to eliminate impurities from liquids or gases. An adsorption isotherm represents graphically the quantity of adsorbate (contaminant) that adheres to the surface of an adsorbent material, correlating with its concentration in the surrounding medium while maintaining a constant temperature. These isotherms can be harnessed to ascertain the adsorption capacity, denoting the utmost quantity of adsorbate that a particular amount of adsorbent can absorb, in addition to revealing the pace at which adsorption transpires **(Wang and Guo, 2020)**.

2.7.1 Langmuir Isotherm

The Langmuir adsorption isotherm is a model used to describe the adsorption of a solute onto a solid adsorbent material. It is named after the French chemist Irving Langmuir, who proposed this model in 1918. The Langmuir isotherm assumes that the adsorption occurs at specific sites on the surface of the adsorbent and that each site can only adsorb one molecule of the adsorbate.

The Langmuir isotherm equation can be written as:

$$q_e = \frac{q_{max}KC_e}{1+KC_e} \qquad\qquad 2.1$$

where q_e is the adsorption capacity of the adsorbent (mg/g), C_e is the equilibrium concentration of the solute in the liquid phase, q_{max} is the maximum adsorption capacity of the adsorbent at saturation (mg/g), and k is a constant related to the affinity of the adsorbent for the solute.

The Langmuir isotherm equation can be rearranged into a linear form by taking reciprocals:

$$\frac{1}{qe} = \frac{1}{qmax} + \frac{1}{K\,qmax} \times \frac{1}{Ce} \qquad\qquad 2.2$$

A plot of $1/q_e$ versus $1/C_e$ should produce a straight line, with the slope equal to $1/q_{max}$ and the intercept equal to $1/K\,q_{max}$.

The Langmuir isotherm is often used to describe the adsorption of solutes onto surfaces that have a limited number of homogeneous, equally accessible sites, such as adsorption onto a metal surface **(Ben-Ali *et al.*, 2017)**.

2.7.2 Freundlich Isotherm

The Freundlich isotherm is a mathematical model that describes the adsorption of a solute onto an adsorbent material. It assumes that the surface of the adsorbent is heterogeneous, with varying energies of adsorption sites, and that the adsorption capacity increases with increasing concentration of the solute in the liquid phase.

The Freundlich isotherm equation is given as:

$$qe = KCe^{1/n} \qquad\qquad 2.3$$

where: q_e is the adsorption capacity of the adsorbent (mg/g), C_e is the equilibrium concentration of the solute in the liquid phase (mg/L) , K is a constant that represents the adsorption capacity , n is an empirical constant that represents the degree of non-linearity of the isotherm.

The Freundlich isotherm equation can be rearranged into a linear form by taking logarithms:

$$log\ q_e = logK + \frac{1}{n} logC_e \qquad\qquad 2.4$$

A plot of *log q_e* versus *log C_e* should produce a straight line, with the slope equal to 1/*n* and the intercept equal to *log K*.

The Freundlich isotherm particularly useful for systems where the concentration of the solute is relatively high, and multilayer adsorption occurs on the surface of the adsorbent. The Freundlich isotherm also provides information about the heterogeneity of the adsorbent surface and the strength of the adsorbate-adsorbent interactions **(Stala, Ulatowska and Polowczyk, 2021)**.

2.7.3 Tamkin Isotherm

The Tamkin isotherm is a mathematical model used to describe the adsorption behaviour on solid surfaces. It is expressed by the equation:

$$qe = (\frac{RT}{bt})\ln K_t + (\frac{RT}{bt})\ln C_e \qquad\qquad 2.5$$

where b_t is constant related to the heat of sorption (J/mol), K_t is the equilibrium binding constant (L/g), *T* is the absolute temperature (K), and *R* is the gas constant. The Temkin isotherm model assumes that the adsorption heat of all molecules decreases linearly with the increase in coverage of the adsorbent surface and that adsorption is characterized by a uniform distribution of binding energies, up to maximum binding energy **(Zhou, Maimaitiniyazi and Wang, 2022)**.

2.8   Kinetic Adsorption

The kinetics of adsorption refers to the rate at which molecules or particles are adsorbed onto a surface over time. It is a dynamic process that depends on various factors, such as the concentration of the adsorbate, the surface area of the adsorbent, and the temperature. The kinetics of adsorption can be described by different models, which typically assume that the adsorption process follows a certain order. The most commonly used models are the pseudo-first-order kinetic model and the pseudo-second-order kinetic model **(Revellame *et al.*, 2020)**.

The pseudo-first-order kinetic model assumes that the rate of adsorption is proportional to the difference between the equilibrium concentration and the concentration of the adsorbate on the surface of the adsorbent.

$$ln(q_e - q_t) = lnq_e - k_1t \qquad\qquad 2.6$$

Where q_e represents the adsorption capacity at equilibrium (mg/g), q_t is adsorption capacity at time t (mg/g), and k_1 (1/min) represents the pseudo-first-order rate constant, t is contact time (min).

The second-order kinetic model assumes that the rate of adsorption is proportional to the product of the concentration of the adsorbate on the surface of the adsorbent and the concentration of the adsorbate in the bulk phase.

$$\frac{t}{qt} = \frac{1}{k2*qe2} + \frac{1}{qe} \qquad\qquad 2.7$$

Where, k_2 (g/mg.min) is the rate constant of the second-order equation and the other terms are as defined previously.

2.9   Previous Work

(He *et al.*, 2016) A series of cross-linked hydrogels were synthesized by dispersive polymerization, incorporating sodium acrylate and acrylamide copolymer with graphene oxide (P(AANa-co-AM)/GO). Scanning electron microscopy (SEM) images displayed a rougher surface on the P(AANa-co-AM)/GO gel. BET analysis indicated a relatively small surface area of 2.07 m^2/g and an average pore volume of 0.12 cm^3/g for the P(AANa-co-AM)/GO gel. This hydrogel exhibited robust tenacity and mechanical strength, essential qualities for a reusable adsorbent in the effective removal of heavy metal ions from practical wastewater applications.

(Liu *et al.*, 2019) Core/shell/shell-like $Fe_3O_4@SiO_2@PPy$ nanospheres were successfully synthesized using a polymerization method. These composite nanospheres consist of iron oxide (Fe_3O_4) as the core, surrounded by a silica (SiO_2) shell and a polypyrrole (PPy) outer shell. The nanospheres are spherical in shape and have a diameter ranging from 110 to 240 nm, smaller than $Fe_3O_4@SiO_2$ microspheres. The thickness of the outer shell is approximately 25 nm. X-ray diffraction (XRD) analysis indicates high crystallization of the Fe_3O_4 core. This newly created composite shows potential for use in microwave absorption applications due to its unique structure.

(Alterary and AlKhamees, 2021) Magnetic iron oxide nanoparticles (Fe_3O_4 NPs) were fabricated using a co-precipitation method, subsequently encased in a protective silica (SiO_2) shield to prevent aggregation. The outcome yielded notable magnetic saturation and stability. XRD diffraction analysis confirmed that the SiO_2 presence did not alter the diffraction pattern peaks, confirming the undisturbed essence of Fe_3O_4. TEM analysis revealed the spherical structure of the synthesized nanoparticles, augmented by a slight enlargement due to the SiO_2 encasement. The surface area measured an impressive 104.8 m2/g. These core-shell $Fe_3O_4@SiO_2$ nanoparticles show great potential for diverse applications in the realms of medicine and environmental science.

(Zhang, He and Zhao, 2021) Magnetic nano catalysts find broad application in organic reactions, capitalizing on their magnetic properties for separation and reuse. A catalyst named $Fe_3O_4@SiO_2$ was modified with diazabicyclo undecene (DBU) and employed in the Knoevenagel reaction. XRD analysis confirmed the formation of $Fe_3O_4@SiO_2@propyl@DBU$, showing amorphous silicon around Fe_3O_4 with characteristic peaks at 18°–28°. The nanoparticles were spherical, sized 10-15 nm, and displayed agglomeration due to magnetism. The BET surface area measured 6.6029 m^2/g. The catalyst significantly enhanced the Knoevenagel reaction—boosting reaction rate and yield—while being easily separated via external magnetic force. Impressively, the catalyst maintained its effectiveness over 10 recycling cycles without any loss of catalytic activity.

(Dehghani *et al.*, 2018) This study aimed to assess the effectiveness of a novel Poly(urea-formaldehyde) adsorbent for eliminating cadmium ions from water solutions. The research analyzed various factors, including initial pH, contact time, initial cadmium concentration, and real wastewater samples. According to the findings, the Langmuir model revealed a maximum adsorption capacity of 76.3 mg/g at pH 5.5. This indicates the adsorbent's superior performance in weakly acidic to near-neutral pH ranges, demonstrating higher adsorption efficiency under such conditions. The removal percentage achieved was 54.5% after 5 minutes. Adsorption efficiency did not considerably change and was mostly stable until the adsorbent was saturated.

(Guleria, Kumari and Lima, 2020) Cellulose biopolymer was chemically modified through graft copolymerization and utilized as an innovative adsorbent for removing harmful inorganic pollutants from wastewater. The resultant adsorbent, Cellulose-g-poly-(acrylamide-co-acrylic acid), was systematically optimized by investigating various parameters, including pH, contact time, temperature, and the concentration of metallic ions. The adsorption experiments encompassed a wide range of metallic ion concentrations (100–1000 mg/L), initial pH values (pH 2–7), and contact times spanning from 5 to 180 minutes. Notably, the adsorbent's maximum monolayer capacity (q_m) was determined to be 101.73 mg/g specifically for Cd^{+2} ions. This research underscores the potential of modified cellulose as an efficient adsorbent for tackling toxic inorganic pollutants in wastewater.

(Aarab *et al.*, 2020) The study details the creation of a polyaniline-polypyrrole (PPY-PANi) copolymer and its application in removing metronidazole from water using batch adsorption trials. The copolymer's surface analysis reveals an irregular and porous granular structure. The impact of varying PPY-PANi doses on adsorption efficiency is investigated, with the highest removal (89.24%) observed at a dose of 0.40 g/L. Beyond this dose, adsorption remains nearly constant. The study also explores the effect of pH on adsorption, finding that acidic conditions (pH $\leq$ 6.2) enhance metronidazole removal. Overall, these findings suggest the promising potential of PPY-PANi copolymer as an effective adsorbent for wastewater treatment.

(Sharma and Naushad, 2020) The study involves the creation of a composite material called datestone activated carbon-based zirconium oxide (DSAC/ZrO_2). The composite has specific properties such as a surface area of 153.4 m²/g, a pore volume of 0.04 cm³/g, and an average pore diameter of 8.8 nm. The research focuses on using this composite to remove cadmium ions through adsorption, employing a batch process where 100 mg of DSAC/ZrO_2 is exposed to a 20 ppm cadmium solution at 25°C. Sampling occurs over various time intervals (0-240 min). The efficiency of cadmium ion removal increases from 21% to 74% as the pH is raised from 2 to 6, but beyond pH 6, removal efficiency decreases. At lower cadmium ion concentrations, more attachment sites are available on DSAC/ZrO_2, leading to higher removal percentages. However, as cadmium ion concentration rises, adsorption diminishes due to saturation of available sites on DSAC/ZrO_2.

CHAPTER 3

EXPERIMENTAL WORK

3.1   Introduction

This chapter has three main sections: the first one explains the chemicals, equipment, and laboratory tools used in this study. The second section describes the preparation of nanocomposite adsorbent, while the last section discusses adsorption and the materials utilized as adsorbate, as well as the influence of variables on batch and continuous systems.

3.2   Chemical and Equipments

3.2.1 Chemicals

All chemicals used in this work are shown in Table 3-1.

Table 3-1: The chemical components used

No.	Chemicals	Formula	Purity%	Manufacturer
1	Ferrous chloride	$FeCl_2.4H_2O$	98	LOBA Chemie, India
2	Ferric chloride	$FeCl_3.6H_2O$	96	Qualikems, India
3	Ammonia hydroxide solution	NH_4OH	25	LOBA Chemie, India
4	Sodium hydroxide	$NaOH$	99	SCHARLAU, Spain
5	Acetone	C_3H_6O	99	IMPLURA, India
6	Ethanol	C_2H_6O	85	Alpha Chemika, India
7	Tetraethyl orthosilicate	$SiC_8H_{20}O_4$	99	Glentham, UK
8	Potassium persulfate	$K_2S_2O_8$	99	E. Merck, Germany
9	Acrylic acid	$C_3H_4O_2$	99	TBCPL, India

10	Acrylamide	C_3H_5NO	98	Sigma-Aldrich, USA
11	4-Aminobenzoic acid	$C_7H_7NO_2$	98	Glentham, UK
12	(3-Aminopropyl) triethoxysilane	$C_9H_{23}NO_3Si$	99	Sigma-Aldrich, USA
13	Hydrochloric acid	HCL	36	ReAgent, UK
14	Cadmium chloride	$CdCl_2.H_2O$	98	TBCPL, India
15	Deionized water	H_2O	/	Local market, Iraq

3.2.2 Equipments

Equipments used for nanocomposite preparation is presented in Table 3-2:

Table 3-2: The equipments used

No.	Apparatus	Description	Manufacturer
1	pH meter	Digital	Hanna Instruents, Australia
2	Thermometer	Digital thermometer with range (-50 -300) ^{o}C, and resolution 0.1 ^{o}C	ASWAR, Iraq
3	Magnetic stirrer with heater	Speed range 60-1500 rpm temperature up to 380°C	Alpha Laboratories, UK
4	Oven	Maximum temperature 220 ^{o}C	Heraeus, UK
5	Centrifuge	Maximum speed 6000 U/min	Hettich, Germany
6	Ultrasonic Mixing	Water bath with ultrasonic source maximum time 30 min	ISOLAB, Germany
7	Digital balance	Maximum weight 220 g minimum weight 0.0001 g	KERN & Sohn GmbH, Germany
8	Filter paper	Pore size 8 μm	China
9	Vacuum pump	Vacuum filtration pump with buchner funnel, and buchner flask	Alcatel, France
10	Dosing pump	Inject a substance into process at a highly accurate flow rate	Guangdong, China
11	Shaker	Used to mix substances in a tube or flask	KOTTERMANN 4010, Germany
12	Other equipment like (beaker, flask, funnel …etc.).	\	\

3.3   Preparation of Nanocompsite Adsorbent

3.3.1 Synthesis of Magnetic Nanoparticles Fe$_3$O$_4$

Magnetic Fe$_3$O$_4$ particles were prepared by the method of co-precipitation **(Emrani *et al.*, 2023)**. FeCl$_3$·6H$_2$O (8.1g) and FeCl$_2$·4H$_2$O (3.4g) were added into a 250 mL round-bottom flask containing 100 mL of distilled water. Under exposure to nitrogen gas, the reaction mixture was stirred at 30°C for 30 min. When all ingredients had dissolved, 13.7 mL of NH$_4$OH was quickly added, and the color of the solution changed rapidly from orange to black. The solid product was collected by filter paper and a vacuum pump and washed with deionized water until the solution remained neutral (pH =7). Then it was washed repeatedly with acetone and ethanol in turn. The remaining solution was dried using the oven at 100 ^{o}C for 24 hours, and the black crystalline particles Fe$_3$O$_4$ were obtained. Figure 3-1 shows the process flow chart, Figure 3-2 show the manufacturing stages from the beginning until obtaining the black crystalline particles Fe$_3$O$_4$.
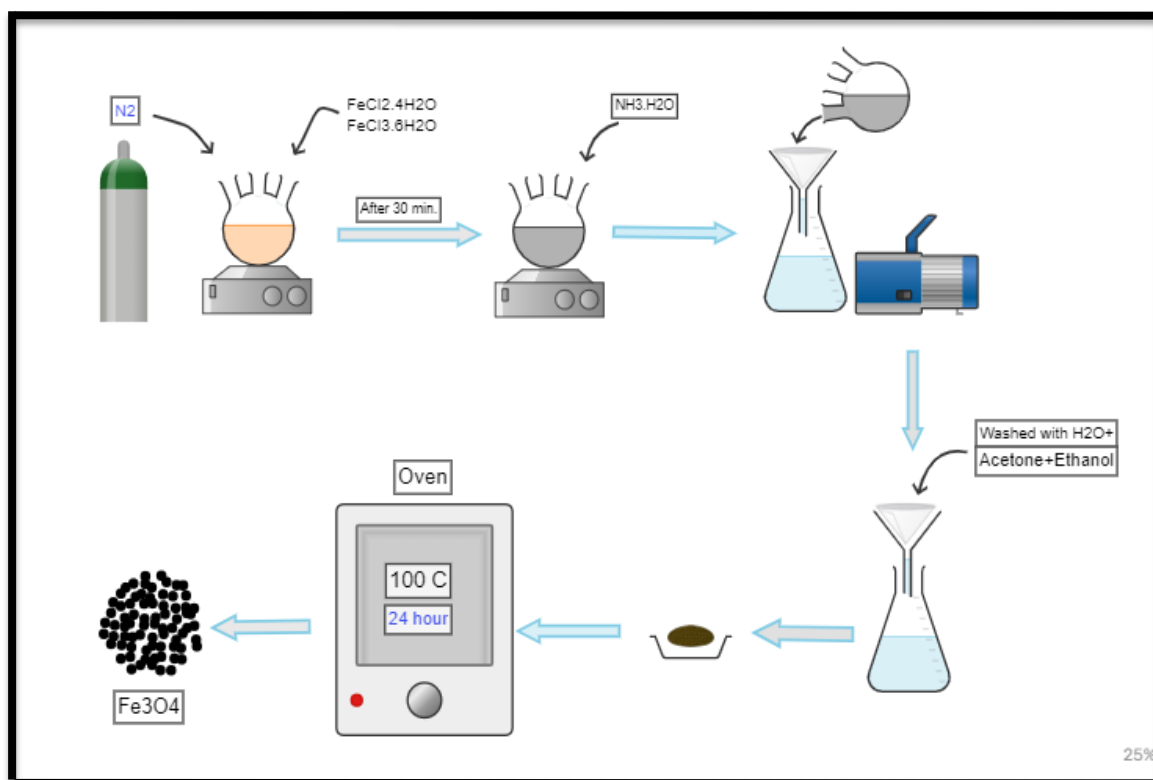
Figure 3-1: Scheme explains the Fe_3O_4 nanocrystals preparation method

Figure 3-2: Steps for synthesis Fe_3O_4 (a) co-precipitation of $FeCl_3 \cdot 6H_2O$ and $FeCl_2 \cdot 4H_2O$ with distilled water. (b) After adding NH_4OH and the color changed to black (c) The solid product collected by filter paper. (d) using vacuum pump. (e) Fe_3O_4 after removing the residual solvent by oven.

3.3.2 Synthesis of Magnetic Nanoparticles $Fe_3O_4@SiO_2$

The core-shell structure $Fe_3O_4@SiO_2$ was produced using a modified Stober technique **(Lu *et al.*, 2008)**. In this approach, a mixture of 20 mL distilled water, 80 mL ethanol, 5 mL tetraethylorthosilicate (TEOS), and 5 mL ammonia solution (NH_4OH, 25%) was combined in a 40°C water bath with mechanical stirring to induce hydrolysis and condensation of TEOS. After 10 minutes, 100 mL (80 mL ethanol and 20 mL water) of a Fe_3O_4 solution containing about 2 g of Fe_3O_4 was added was sonicated and added to the aforementioned mixture. The reaction proceeded at room temperature for 12 hours, during which the resulting products were collected using a magnet. Subsequently, they were neutralized with distilled water and ethanol, followed by re-dispersion in a solution comprising 160 mL ethanol, 40 mL distilled water, and 4 mL ammonium hydroxide (25%) for subsequent utilization.

3.3.3 Synthesis of $Fe_3O_4@SiO_2$-M

The APTES/$Fe_3O_4@SiO_2$ ($Fe_3O_4@SiO_2$-M) composite was prepared by further modifying $Fe_3O_4@SiO_2$ using a silane coupling agent (APTES). The specific experimental procedure was conducted as follows: 4 mL of APTES was introduced into the aforementioned $Fe_3O_4@SiO_2$ solution and subjected to mechanical stirring for 24 hours in a water bath at 60^oC. The mixture was then allowed to cool naturally to room temperature. The resulting product was collected using a magnet, washed extensively with distilled water and ethanol through repeated cycles, and subsequently dried in a vacuum oven at 60^oC. Figure 3-3 shows the manufacturing steps of $Fe_3O_4@SiO_2$-M **(Liu, Wang and Zhang, 2020).**

Figure 3-3: Steps for synthesis $Fe_3O_4@SiO_2$

3.3.4 Loading Polymer on $Fe_3O_4@SiO_2$-M

Two different polymers were prepared, the first one is; P1. To produce acrylic acid with a neutralization degree of 0.8, an initial step involved using sodium hydroxide in a water bath maintained at 5°C. The forthcoming section provides a comprehensive overview of the standard process employed for the fabrication of P1 composite. This composite was synthesized using an AA/PABA mass ratio of (1:1). The outlined procedure is as follows: 4 g of $Fe_3O_4@SiO_2$ underwent sonication in 100 mL of distilled water for a duration of 30 minutes. The resulting solution was then transferred to a 250 mL three-neck flask containing 25 mL of AANa solution comprising 10 ml of AANa, 10 ml of Para-aminobenzoic acid (PABA), and 0.2 ml of the cross-linking agent (TEOS). The flask was purged with nitrogen gas for 15 minutes. Following that, 20 mL of a $K_2S_2O_8$ solution containing 0.4 g of $K_2S_2O_8$ in water was added to the flask, and the mixture was heated to 55°C for a period of 1.5 hours. Lastly, the obtained P1 composite were fragmented and immersed in a mixture of ethanol and water (in a 1:1, v/v ratio) for a duration of 24 hours to remove any residual unreacted monomers. The resulting product was then dried in a vacuum oven at 60°C for 7 hours.

The second polymer P2; which was prepared in the same way as the first polymer loading, the difference is that 10 ml of AM was used instead of PABA. Figure 3-4 and 3-5 shows the polymers synthesis steps and schematic synthesis of the nanocomposites respectively.
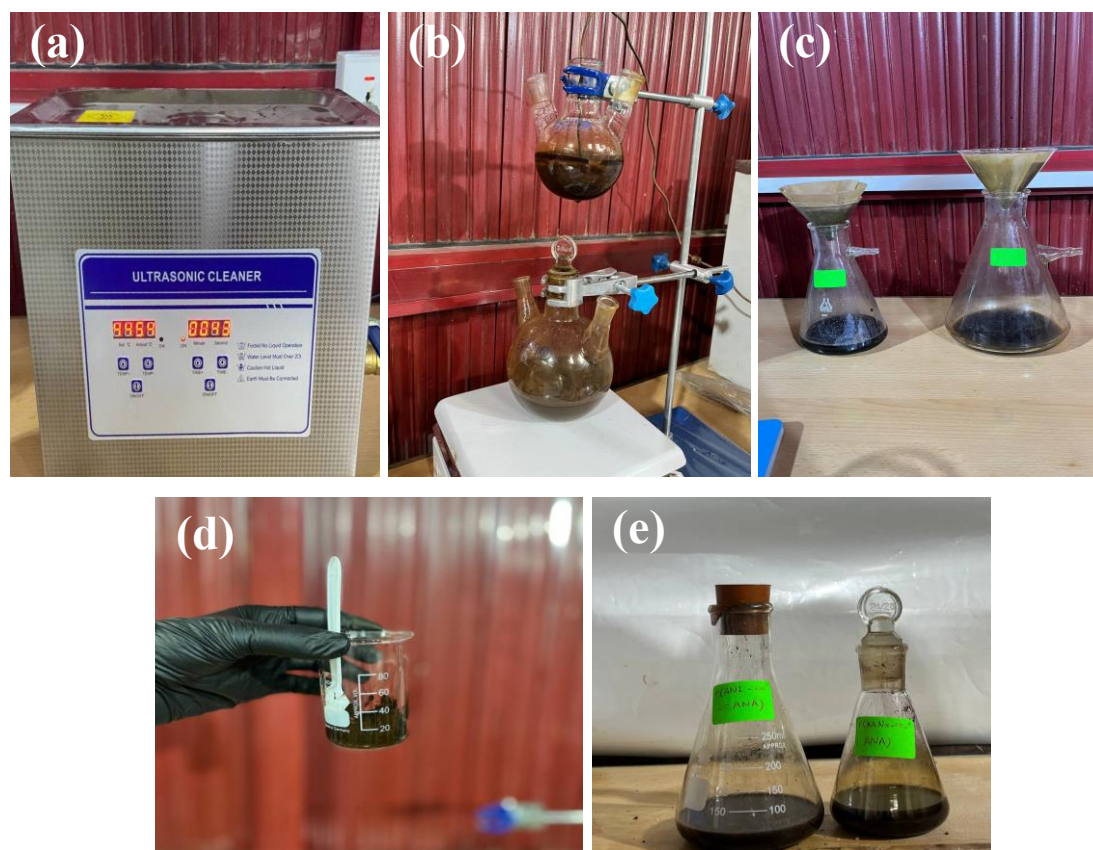
Figure 3-4 : Steps for synthesis the polymers
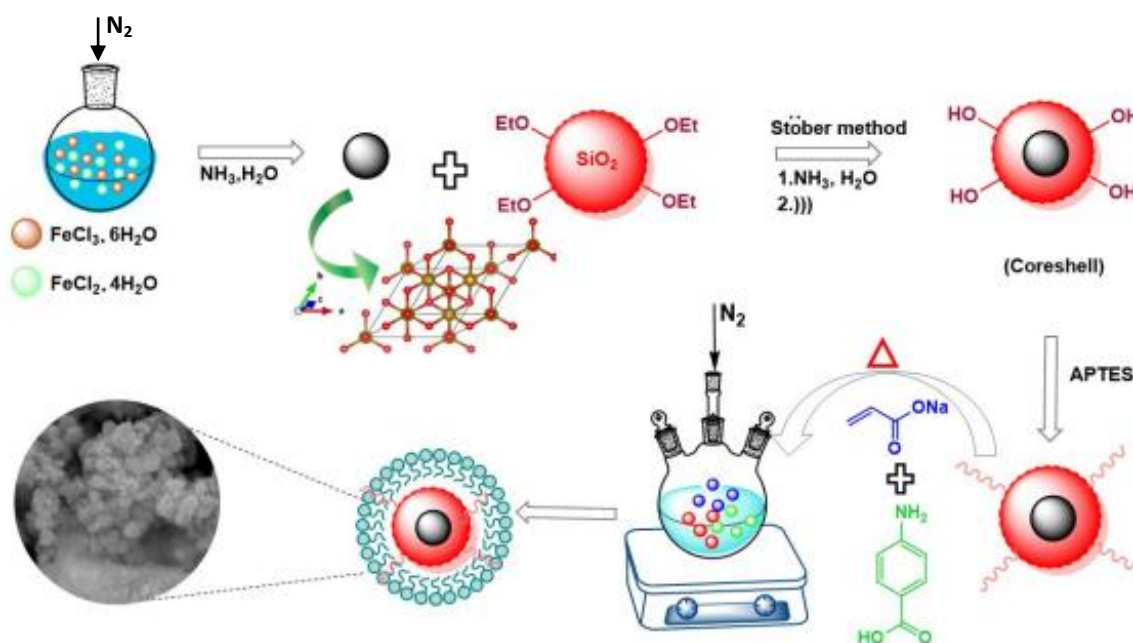
Figure 3-5: Schematic synthesis of the nanocomposites

3.4   Preparation of Stock Solution

A standard stock solution was prepared at room temperature. For Cadmium(II) ions, stock-aqueous solution of 1000 mg/L was made by dissolving 0.44 g of $CdCl_2.H_2O$ (molar mass is 201.3 g/mol) in 1000ml deionized water, then different concentrations of Cd(II) were made by appropriate dilutions of the stock solution of standards aqueous with suitable capacities of deionized water. The pH of the solution was adjusted with NaOH and HCL.

3.5   Adsorption Experiments

3.5.1 Batch Experiments

For batch experiments, shaker operating at 120 rpm was used at room temperature. The adsorption of P1 and P2 was examined over a duration of 405 minutes, 100 ppm concentration of Cd(II) solution and 0.3 g of adsorbent were placed in a 100 mL round bottom flask to facilitate adsorption. The impact of contact time on adsorption was investigated by varying the duration (from 5 to 405 minutes). While the mass of the catalyst used in the experiments ranged (from 0.05 to 0.3 g). To establish the adsorption isotherm, the initial concentration of cadmium ranging (from 25 to 150 ppm). The effect of different aqueous pH values ranging (from 2.5 to 12). The pH value yielding the best results was chosen for all subsequent tests. Following filtration, the concentration of cadmium ions was measured using an atomic absorption spectrophotometer as shown in Figure 3-6.

The equilibrium adsorption capacity q_e (mg/g) and the removal rate *(R%)* of Cd(II) were calculated by equations 3.1 and 3.2, respectively :

$$q_e = \frac{(Co - Ce)V}{m} \qquad\qquad 3.1$$

$$\boldsymbol{R}\ (\%) = \frac{Co - Ce}{Co} \times 100\% \qquad\qquad 3.2$$

where C_o and C_e are the initial and the final concentrations (mg/L), respectively, V is the volume of the solution (L), and m is the dry weight of the adsorbent (g).

Figure 3-6: Batch adsorption experiments

3.5.2 Factors Controlling the Adsorption Process

▪ **Effect of Time**

The effects of contact time on the adsorption effectiveness was studied at 25C° for 5, 15, 30, 45, 90, 180, 270, 360,and 405 min. The Cadmium ions concentrations 100 ppm, adsorbent dosages 0.3 g and pH 8. After the end of the last time, 405 minutes, the remaining concentration of cadmium ions was measured using AAS.

- **Effect of Dose**

    In this experiment , the impact of adsorbent weight on adsorption was investigated using various doses of adsorbent 0.05, 0.1, 0.15, 0.2, 0.25, and 0.3 g, a fixed concentration of 100 ppm of cadmium, at constant agitation speed (120 rpm) for 405 min, and pH 8 at room temperature in round bottom flasks of 100 ml. Centrifugation, filtration, and an Atomic Absorption Spectroscopy were used to measure and evaluate the residual cadmium content in the solution (AAS).

- **Effect of pH**

    Adsorption experiments were carried out as a function of pH using a steady concentration of 100 ppm of cadmium with 0.3g of adsorbent at constant agitation speed (120 rpm) for 405 minutes at room temperature in round bottom flasks 100 ml. Various amounts of NaOH and HCL were added to each sample's solution pH to a specified value between 2.5, 4, 8, 10, and 12 using a pH meter. The residual cadmium content in the solution was measured using centrifuge, filtering, and an Atomic Absorption Spectrometry (AAS).

- **Effect of Concentration**

    In this experiment, the impact of adsorbate concentration on adsorption was evaluated using different concentrations of cadmium of 25, 50, 75, 100, 125, and 150 ppm and a constant dose of adsorbent 0.3 g at constant agitation speed (120 rpm) for 405 minutes and pH 8 at room temperature in round bottom flasks 100 ml. Centrifugation, filtration, and an Atomic Absorption Spectrometry (AAS) were used to measure the residual cadmium content in the solution.

3.5.3 Continuous Experiments

Adsorption continuous experiments were carried out at room temperature using a glass column with a height of 30 cm and an inner diameter of 0.8 cm. The experiments started with making a stock solution with varied concentrations (50, 100, and 150 ppm) of cadmium ions and a constant pH of 8. The solution is injected into the glass column by a dosing pump at a rate of (5,10 mL) per minute under atmospheric pressure. The column is made up of a layer of glass wool under the catalyst and two layers of stones above and below the bed to prevent the adsorbents from dropping. It comprises adsorbents of varying heights (1, 1.5, 2 cm). The cadmium metal ion experiment lasts 270 minutes. The solution is pumped within the column, and a sample is taken from the bottom of the column at a specified time and measured using an atomic absorption spectroscopy (AAS). Figure 3-8 describes continuous experimentation.
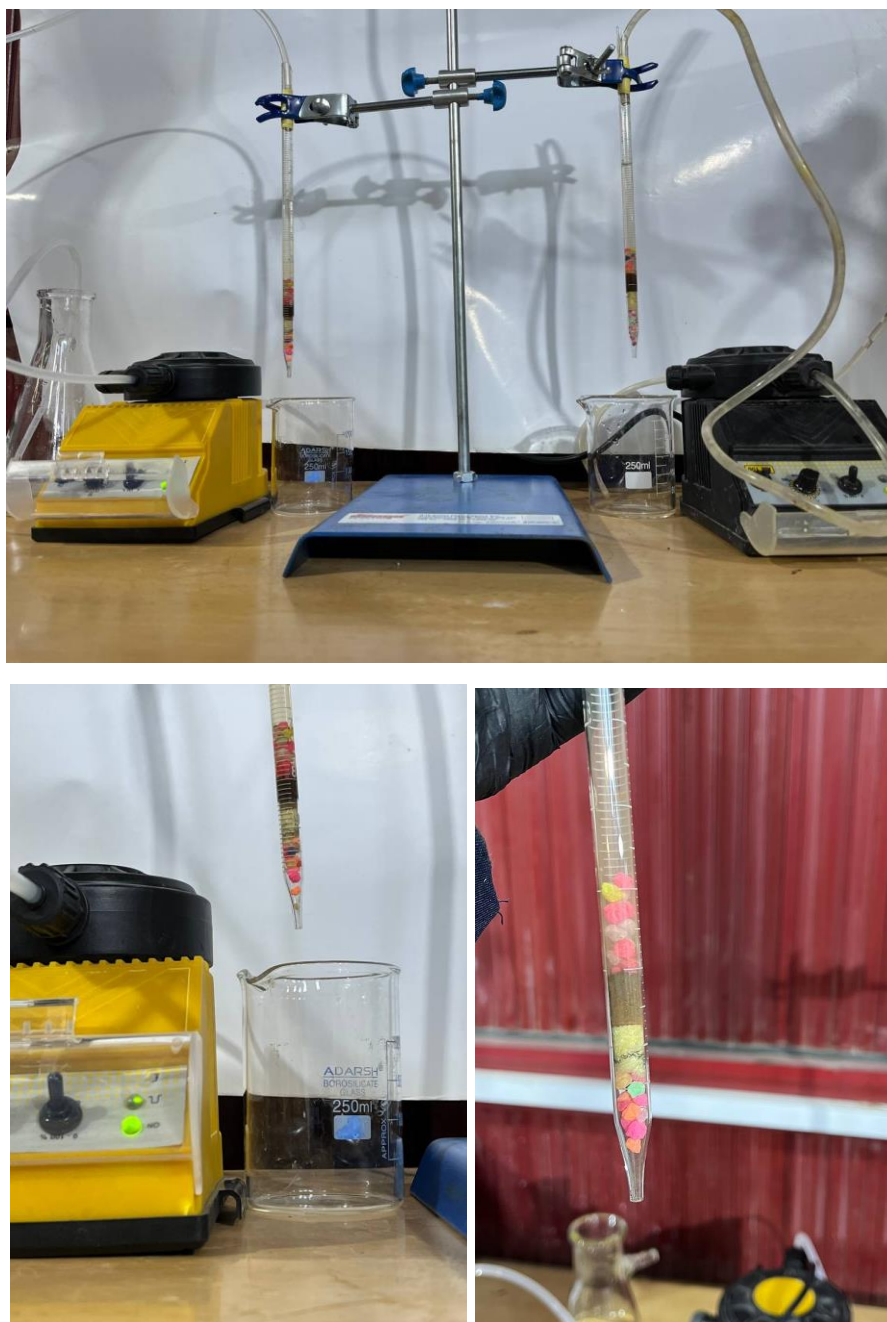
Figure 3-7: Continuous adsorption experiments

3.6   Characterizations

3.6.1 X-Ray Diffraction (XRD)

Used to analyse the crystalline phase and structure of Fe_3O_4 and $Fe_3O_4@SiO_2$ synthesized materials as well as the composites P1 and P2. X-ray diffraction technique was done in (Iraq, Al-Nahrain University/ Physics Sciences Department) using (Panalytical X'Pert Pro / Made in Netherlands).

3.6.2 Field Emission Scanning Electron Microscopy (FESEM) and Energy Dispersive Spectroscopy (EDX)

FESEM was used to investigate the morphological properties of the synthesized catalysts ; P1 and P2. In addition, these samples were exposed to EDX analysis to determine the components of the sample and their composition. FESEM was done In Iran, Tehran University,(Model: Hitachi S-4800, Japan)

3.6.3 Transmission Electron Microscopy (TEM)

TEM was used to study the inner structure, contact form of composites and morphology. The experiment was carried out using a high resolution transmission electron microscope (HR-TEM) on a JEM-2100 electron microscope at an acceleration voltage of 200 Kv. TEM technology done In Iran, Tehran University, (Hitachi, Japan).

3.6.4 Atomic Force Microscopy (AFM)

AFM was used to evaluate the roughness of the catalyst surface. This method generates two and three-dimensional profile pictures. Moreover, items seen by AFM do not require any specific treatments (such as metal/carbon coatings) that might irreversibly modify or harm the sample, and the resulting picture does not often suffer from charging errors. Forces between a sharp cantilever tip and the surface at a very small distance are used to measure the surface on nanoscale. AFM was done at AL-Nahrain University/Chemistry Science Department, (Scanning Probe Microscope, model AT3000, Angstrom, Advanced Inc/ USA).

3.6.5 Fourier-Transform Infrared Spectroscopy (FTIR)

Fourier Transform Infrared Spectroscopy is a way to recognize organic, polymeric, and, in certain situations, inorganic materials. The FTIR analysis method scans test materials using infrared light to evaluate chemical characteristics. All spectra were taken in the (400-4000 cm^{-1}) spectrum. The FTIR analysis was carried out for both of P1 and P2 before and after Adsorption , at Al-Nahrain University/ College of Science/ Chemistry Science Department, the gadget model is (ALPHA FTIR Routine Spectrometer, Bruker, USA).

3.6.6 Brunauer–Emmett–Teller (BET) Surface Area

The specific surface area, pore size, and pore volume of polymers: P1 and P2 were determined using the BET technique using the N_2 adsorption/desorption isotherm. This test was done in In Iran, Tehran University, (Quantachrome Autosorb-6Isa, USA).

3.6.7 Atomic Absorption Spectroscopy (AAS)

Atomic absorption spectroscopy is a spectro-analytical technique used to determine the quantitative properties of chemical elements. In ecology, the approach employs the absorption of optical radiation by free atoms in the gaseous state to determine the specific element concentration for the investigated materials. Almost 70 distinct elements may be determined using AAS in solution or directly in solid materials. It was carried out in Iraq, University of Baghdad/Collage of science/Biology Sciences Department, (Perkin Elmer 1100B, USA).

CHAPTER 4

RESULTS AND EXPLANATION

4.1   Introduction

This chapter focuses on describing the characterizations of the prepared catalysts by XRD, FE-SEM, EDX, BET, AFM, FT-IR, and TEM techniques and describe how different factors affect the adsorption process, as well as the adsorption isotherm and kinetic studies.

4.2   Characterization

4.2.1 X-Ray Diffraction (XRD) Analysis

XRD was used to evaluate the change in crystalline structure of Fe_3O_4 following surface modification. Figure 4-1 displays the X-ray diffraction patterns of Fe_3O_4, $Fe_3O_4@SiO_2$, P1 and P2. The pure Fe_3O_4 planes (220), (311), (400), (422), (511), and (440) were given the six typical peaks at 30.4°, 35.9°, 43.5°, 54.0°, 57.4°, and 63.2°. The similarity of the XRD patterns of Fe_3O_4 and $Fe_3O_4@SiO_2$, as well as the occurrence of all distinctive peaks of Fe_3O_4 in $Fe_3O_4@SiO_2$, demonstrates that coating with SiO_2 layer did not modify the crystallinity structure of Fe_3O_4 because of the amorphous behaviour of SiO_2 **(Zarei, Saedi and Seidi, 2018) (Alterary and AlKhamees, 2021)**. The large peak at $2\theta = 35.4$ with intensity about 83.6 , and 103.7 in the final products , this decrease in intensity attributable to the P1 and P2 layer, confirms the effective synthesis of the P1 and P2 nanocomposites **(Hua and Li, 2014)**.
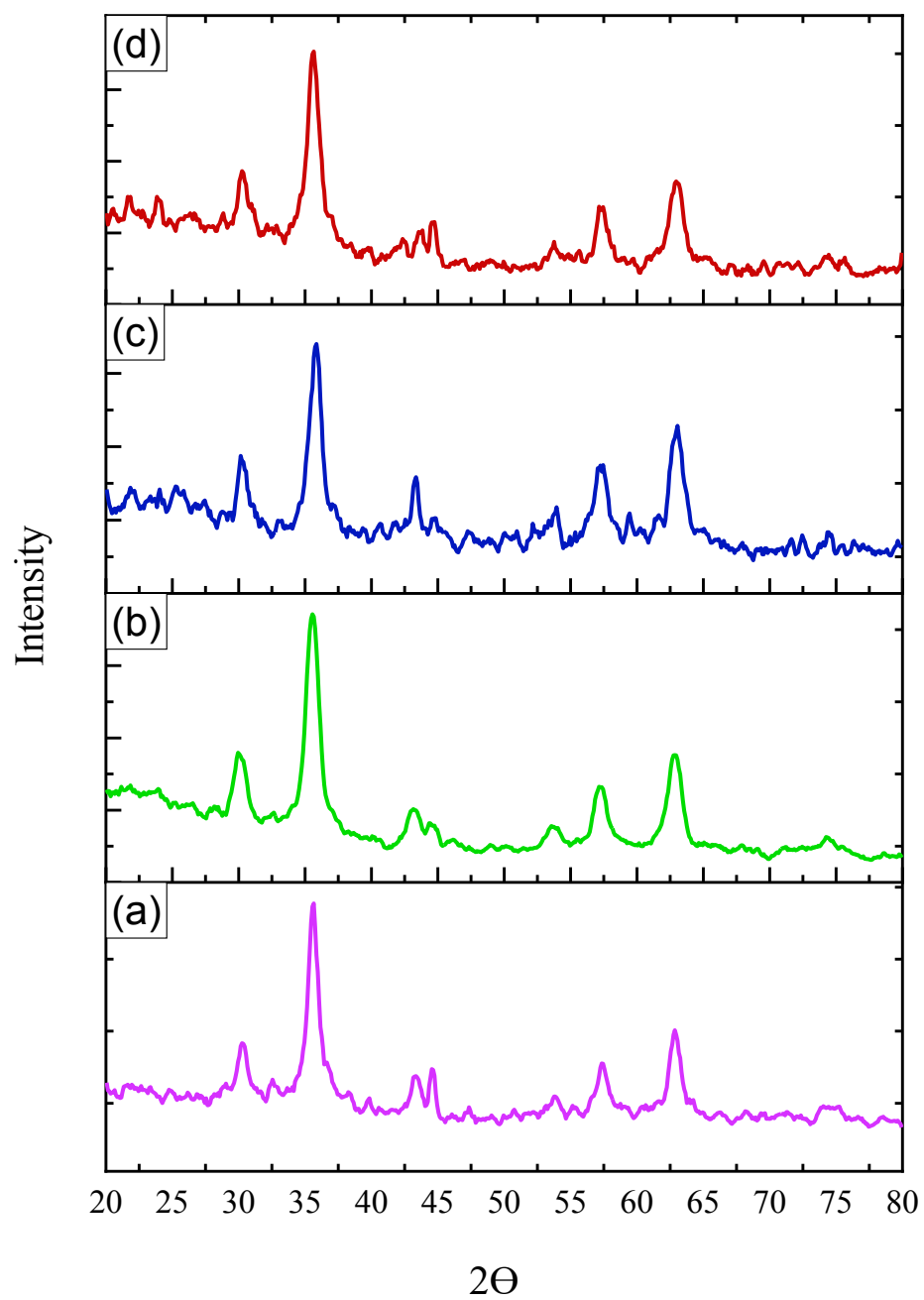
Figure 4-1 : XRD patterns of (a) Fe_3O_4, (b) $Fe_3O_4@SiO_2$, (c) P1, (d) P2

4.2.2 Field Emission Scanning Electron Microscopy (FE-SEM) and Energy Dispersive X-Ray Analysis (EDX)

FE-SEM was used to examine the morphology of the catalyst. Figure 4-2 shows that the average size of P1 nanoparticle is approximately 29.13 nm, while the average size of P2 nanoparticle is around 14.66 nm represented in Figure 4-3. The two composites have a relatively spherical-like shape, sharp edges and rough morphology, which provides a favorable platform for heavy metal adsorption. The agglomeration effect is caused by their magnetic influence, which therefore gives the magnetic nano catalyst easily detached.
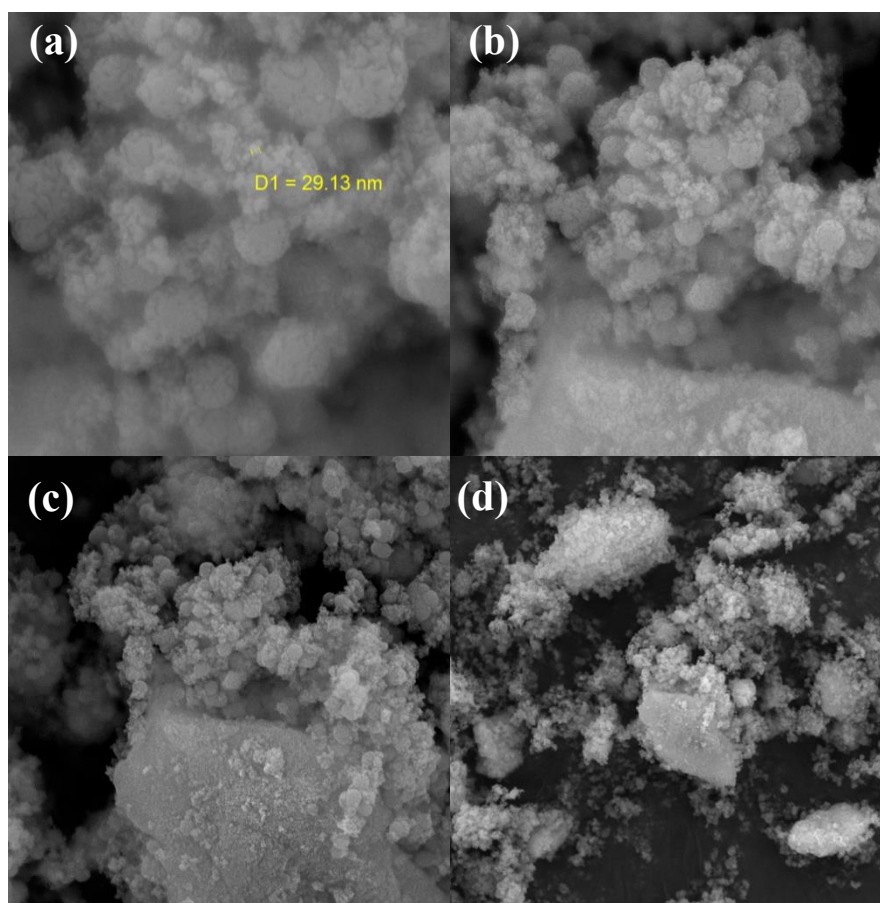
Figure 4-2: The FE-SEM images for P1
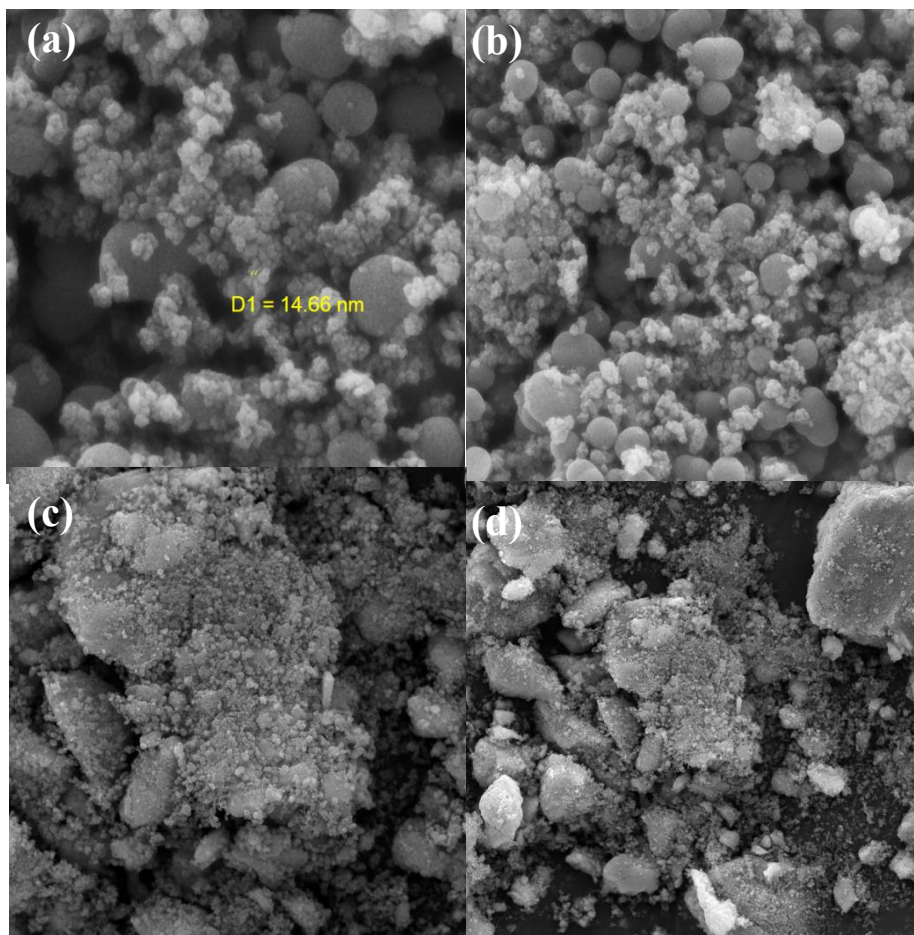
Figure 4-3: The FE-SEM images for P2

The energy dispersive X-Ray analysis (EDX) mention in Figures 4-4, 4-5 identified the elemental composition of the two nanocomposites P1 and P2. the presence of the elements O, Fe, and Si confirms the core-shell $Fe_3O_4@SiO_2$ nanoparticles. The elementary components C, N and Na support the coverage of the $Fe_3O_4@SiO_2$ nanoparticle. Furthermore, no impurity peaks are detected, meaning that the samples is extremely pure as shown in Appendix A.
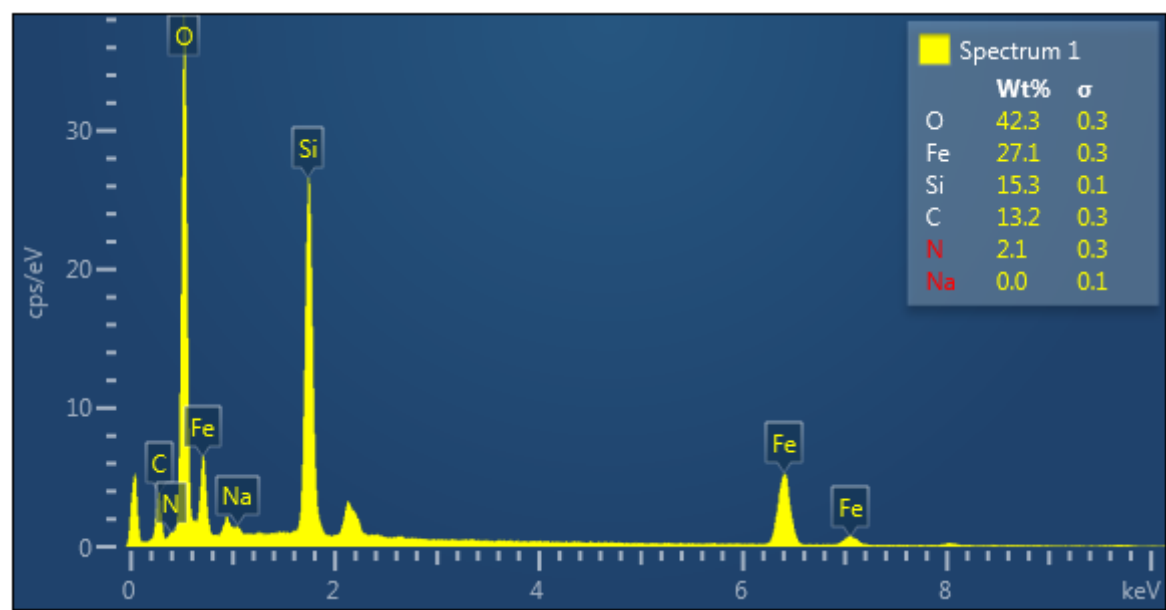
Figure 4-4: The EDX analysis for P1 nanocomposite
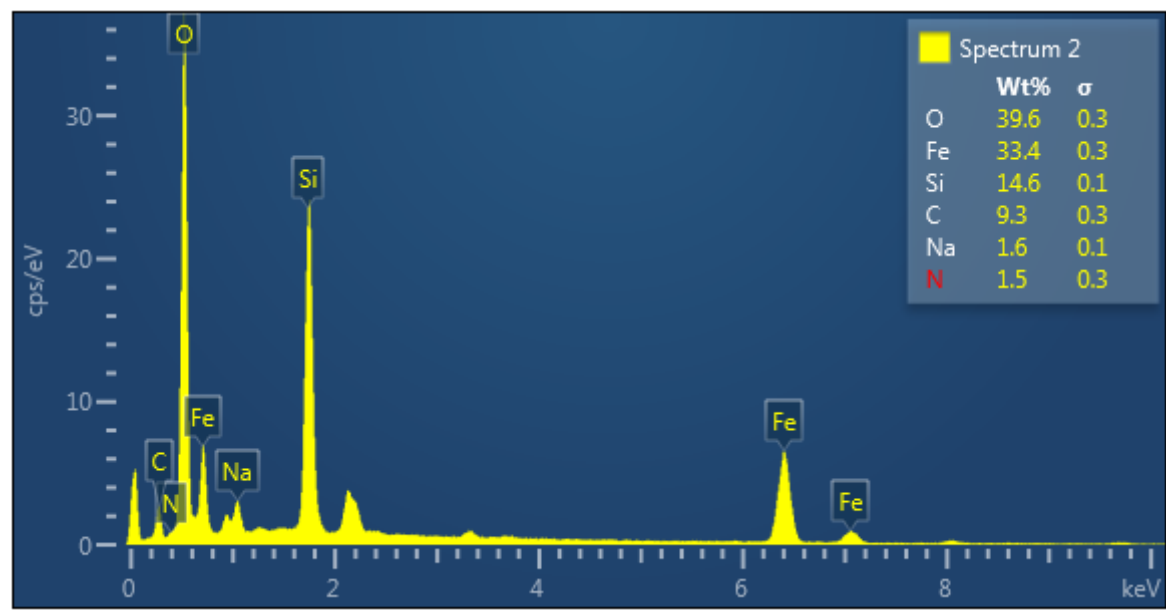
Figure 4-5: The EDX analysis for P2 nanocomposite

4.2.3 Brunauer, Emmett, and Teller (BET) Surface Area Analysis

The BET test employs N_2 for the adsorption/desorption process in order to determine the pore volume and determine the BET surface area. As seen in Figure 4-6, P1 and P2 represents typical IV isotherms according to the IPUAC classification with mesoporous surfaces.
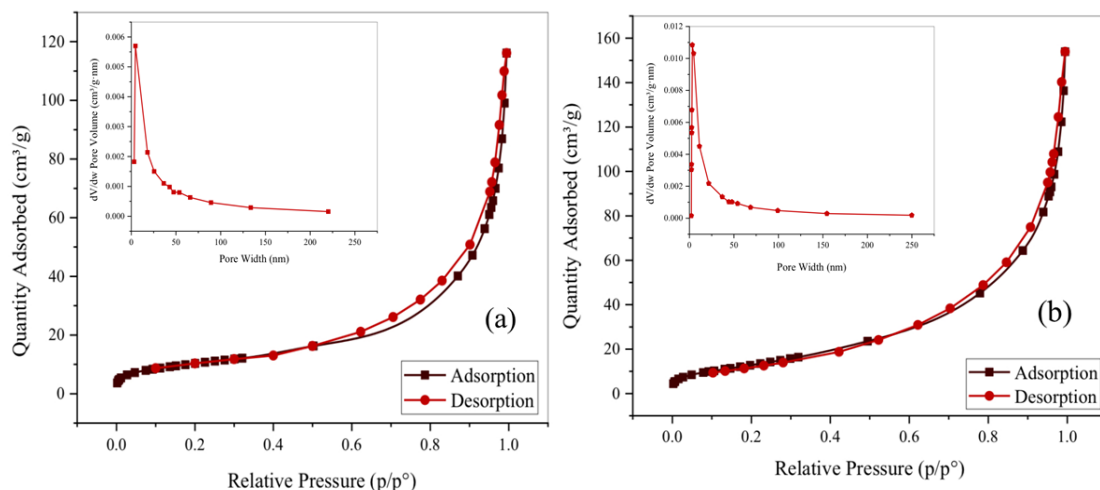
Figure 4-6: (a) N_2 adsorption-desorption and pore size distribution curve (BJH method) for P1, (b) N_2 adsorption-desorption and pore size distribution curve (BJH method) for P2

The presence of a mesoporous pore structure in nanocomposites is supported by hysteresis loop styles that exist in the high relative pressure zone (P/P^o is 0.5~1.0) **(Hazra *et al.*, 2018)**. P1 has a specific surface area of 37.7118 m²/g , a pore volume of 0.105282 cm³/g, and a pore size of 11.16706 nm. While for P2 , the specific surface are 51.3267 m²/g, pore volume 0.146743 cm³/g, pore size 11.43596 nm. The largest pore diameter peak is found in lengths ranging from 2 to 6 nm.

4.2.4 Fourier-Transform Infrared Spectroscopy (FTIR)

The (FT-IR) of both nanocomposite share the following peaks; as seen in Figures 4-7 and 4-8. The peak at 570 cm^{-1} is the typical peak of the Fe–O bond stretching vibration, whereas the wide peak at 1069 cm^{-1} belongs to the Si–O–Si stretching vibration. This indicates SiO_2 effectively coated Fe_3O_4 particles. Besides, at 801 cm^{-1} may indicate to N–C vibration for secondary amines, which suggests the successful binding of $Fe_3O_4@SiO_2$-APTES and the copolymers **(Nawaz *et al.*, 2020)**. The peak at 1661 cm^{-1} relates to the telescopic vibration of the carbonyl and C=O groups. The pre- and post-adsorption spectral lines reveal large and blunt peaks around 2981-3489 cm^{-1}, confirming the existence of association –OH. Figure 4-7 further shows that the peaks at 1500 cm^{-1} and 1380 cm^{-1} are compatible with the symmetric and anti-symmetric telescopic peaks of COO^-. After the adsorption of Cd(II) by P1, the peaks at 1500 cm^{-1} and 1380 cm^{-1} shifted to 1490 cm^{-1} and 1378 cm^{-1}, which is a result of the interaction between Cd and –OH and formation of Cd–OH band.
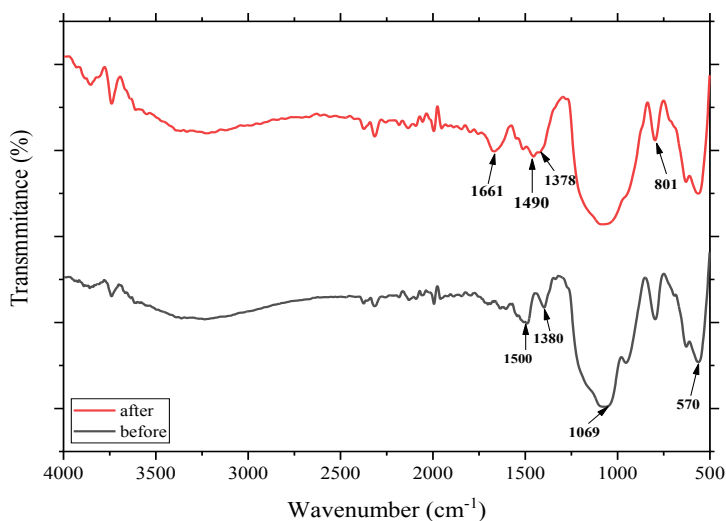
Figure 4-7 : FT-IR spectra for P1 nanocomposite before and after adsorption

For P2, after the adsorption of Cd(II) , the peaks at 1502 cm^{-1} and 1530 cm^{-1} shifted to 1496 cm^{-1} and 1525 cm^{-1} Figure 4-8, which may be also due to interaction between Cd and –OH .
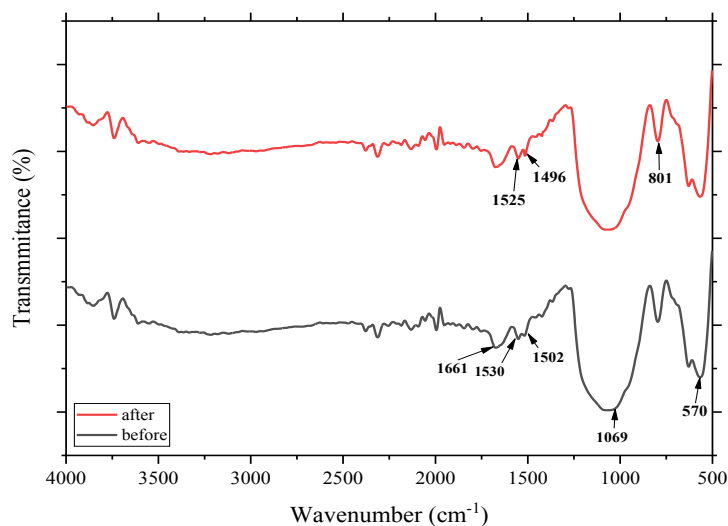
Figure 4-8 : FT-IR spectra for P2 nanocomposite before and after adsorption

4.2.5 Atomic Force Microscope (AFM)

By using an AFM scanning probe microscope, the synthesized nanocomposites particle size distribution and shape were examined. AFM images displayed the layer formation of crystals with their heights and crystal surfaces at the nanoscale. Figure 4-9(a) shows three dimensional image for P1 which is triangular and sharp tip structure. Figure 4-9(b) and Table 4-10 depicts the particle size distribution of the nanocomposite, which confirms that the particle size range of synthesized P1 is (32-58 nm) with an average diameter of 36.11 nm.
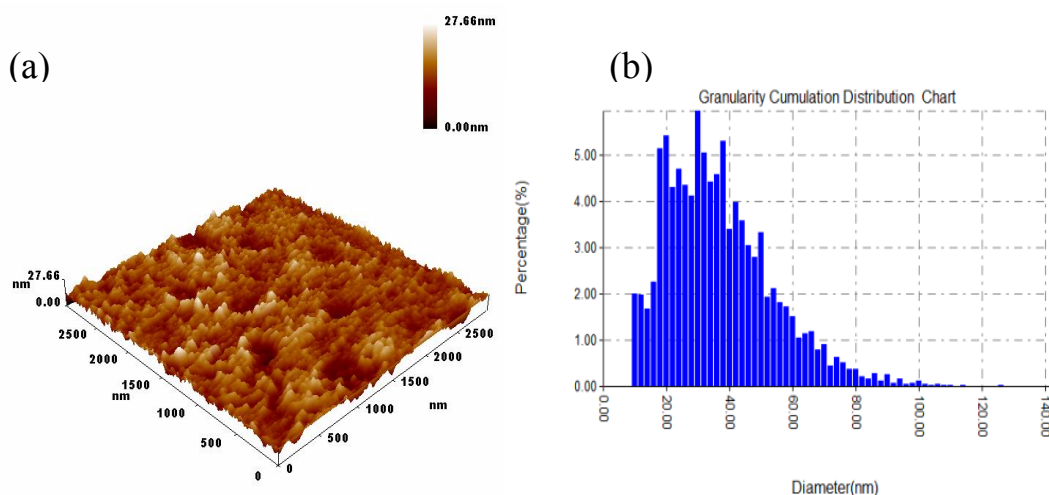
Figure 4-9: AFM three dimensional image and granularity accumulation distribution for sample P1

Avg. Diameter:36.11 nm						<=10% Diameter:16.00 nm		
<=50% Diameter:32.00 nm						<=90% Diameter:58.00 nm		

Diameter(nm) <	Volume(%)	Cumulation(%)	Diameter(nm) <	Volume(%)	Cumulation(%)	Diameter(nm) <	Volume(%)	Cumulation(%)
10.00	2.01	2.01	48.00	2.79	78.10	86.00	0.29	98.73
12.00	1.98	3.99	50.00	3.33	81.43	88.00	0.14	98.86
14.00	1.69	5.68	52.00	1.93	83.36	90.00	0.26	99.13
16.00	2.26	7.94	54.00	2.13	85.50	92.00	0.09	99.22
18.00	5.14	13.08	56.00	1.81	87.31	94.00	0.17	99.39
20.00	5.42	18.50	58.00	1.72	89.03	96.00	0.06	99.45
22.00	4.31	22.81	60.00	1.52	90.54	98.00	0.09	99.54
24.00	4.70	27.51	62.00	1.06	91.60	100.00	0.12	99.66
26.00	4.34	31.85	64.00	1.15	92.76	102.00	0.06	99.72
28.00	4.13	35.98	66.00	1.20	93.95	104.00	0.03	99.75
30.00	5.94	41.92	68.00	0.80	94.75	106.00	0.06	99.82
32.00	5.05	46.97	70.00	0.91	95.66	108.00	0.03	99.85
34.00	4.42	51.39	72.00	0.46	96.12	110.00	0.03	99.88
36.00	4.59	55.98	74.00	0.63	96.75	114.00	0.05	99.92
38.00	5.31	61.29	76.00	0.52	97.27	126.00	0.05	99.97
40.00	3.39	64.68	78.00	0.38	97.65	136.00	0.02	99.98
42.00	3.98	68.66	80.00	0.38	98.04	142.00	0.02	100.00
44.00	3.59	72.25	82.00	0.23	98.27			
46.00	3.05	75.30	84.00	0.17	98.43			

Table 4-1: Particle size distribution with average diameter for sample P1

Figure 4-10(a) shows three dimensional image for P2 nanocomposite which is dissimilar bumpy structure. The particle size distribution of the nanocomposite is depicted in Figure 4-10 (b) and Table 4-11, confirming that the particle size range of produced P2 is (32-58 nm) with an average diameter of 36.30 nm.
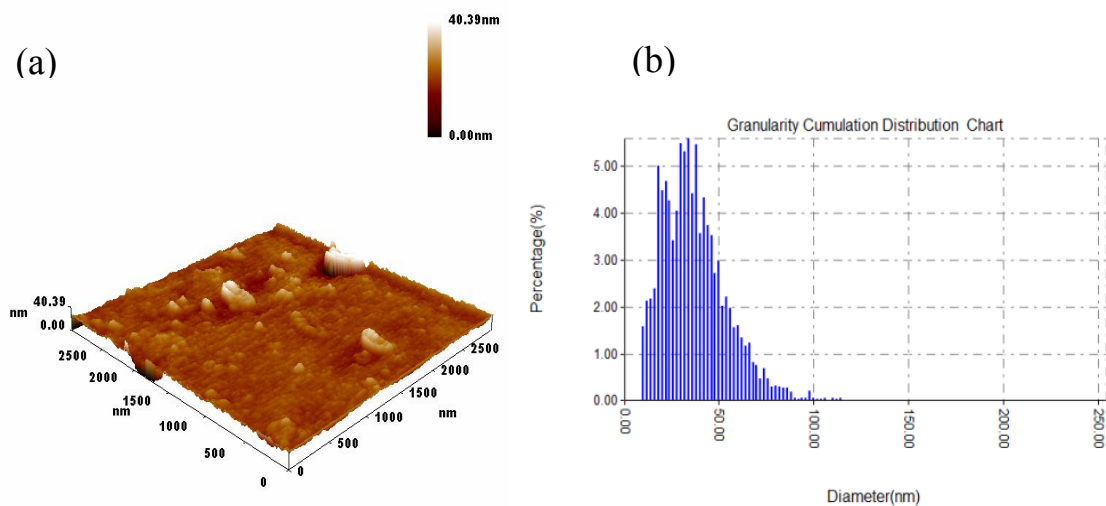
Figure 4- 10: AFM three dimensional image and granularity accumulation distribution for sample P2

Table 4-2: Particle size distribution with average diameter for sample P2

Avg. Diameter:36.30 nm			<=10% Diameter:16.00 nm					
<=50% Diameter:32.00 nm			<=90% Diameter:58.00 nm					
Diameter(nm) <	Volume(%)	Cumulation(%)	Diameter(nm) <	Volume(%)	Cumulation(%)	Diameter(nm) <	Volume(%)	Cumulation(%)
10.00	1.58	1.58	48.00	2.71	78.27	86.00	0.28	99.04
12.00	2.13	3.71	50.00	2.98	81.26	88.00	0.19	99.23
14.00	2.17	5.88	52.00	2.01	83.27	90.00	0.06	99.29
16.00	2.38	8.26	54.00	2.21	85.48	92.00	0.03	99.32
18.00	5.00	13.25	56.00	1.98	87.46	94.00	0.05	99.37
20.00	4.48	17.74	58.00	1.56	89.02	96.00	0.06	99.43
22.00	4.69	22.42	60.00	1.61	90.63	98.00	0.22	99.64
24.00	4.27	26.69	62.00	1.35	91.97	100.00	0.06	99.71
26.00	3.40	30.10	64.00	1.16	93.13	102.00	0.03	99.74
28.00	4.05	34.15	66.00	1.24	94.37	104.00	0.03	99.77
30.00	5.47	39.62	68.00	0.82	95.19	106.00	0.05	99.81
32.00	5.30	44.93	70.00	0.76	95.95	110.00	0.05	99.86
34.00	5.58	50.51	72.00	0.48	96.43	112.00	0.03	99.89
36.00	4.42	54.93	74.00	0.68	97.11	114.00	0.06	99.95
38.00	5.46	60.39	76.00	0.48	97.59	124.00	0.02	99.97
40.00	3.57	63.97	78.00	0.29	97.88	164.00	0.02	99.98
42.00	4.33	68.30	80.00	0.31	98.19	254.00	0.02	100.00
44.00	3.74	72.04	82.00	0.29	98.48			
46.00	3.53	75.56	84.00	0.28	98.76			

4.2.6 Transmission Electron Microscopy (TEM)

The surface morphology of P1 nanocomposite was studied using TEM Figure 4-11, and for P2 nanocomposite Figure 4-12 , As shown in the two figures, the two composites are convergent, two distinct regions with varying electron concentrations can be seen, demonstrating the creation of the core-shell structure. The silica shell was at the border of the gray area, while the Fe_3O_4 core was in the center of the black part. This demonstrates that SiO_2 effectively coats Fe_3O_4 particles **(Liu, Wang and Zhang, 2020)**.
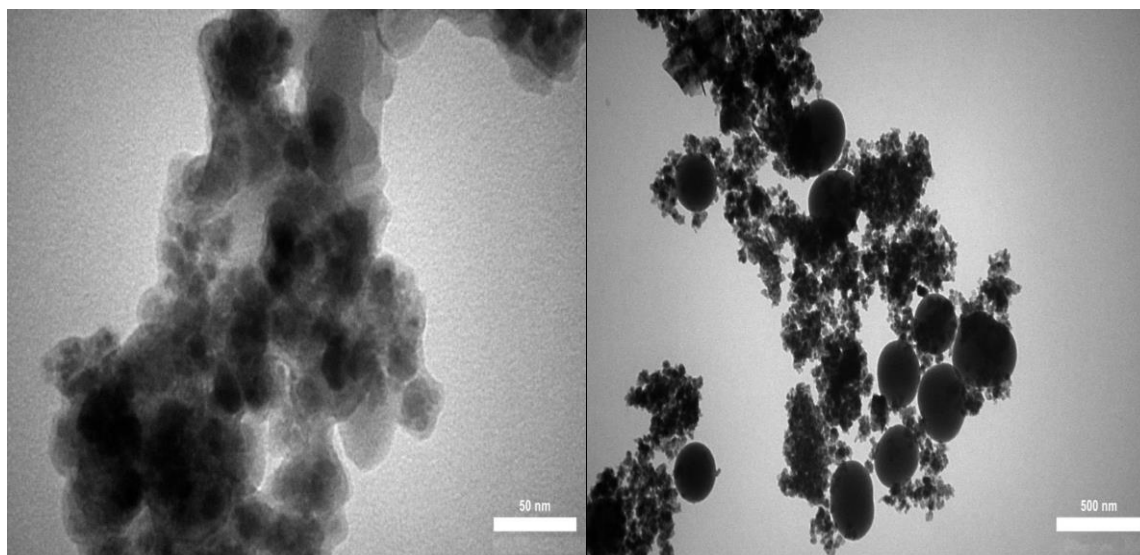
Figure 4-11: TEM picture of P1
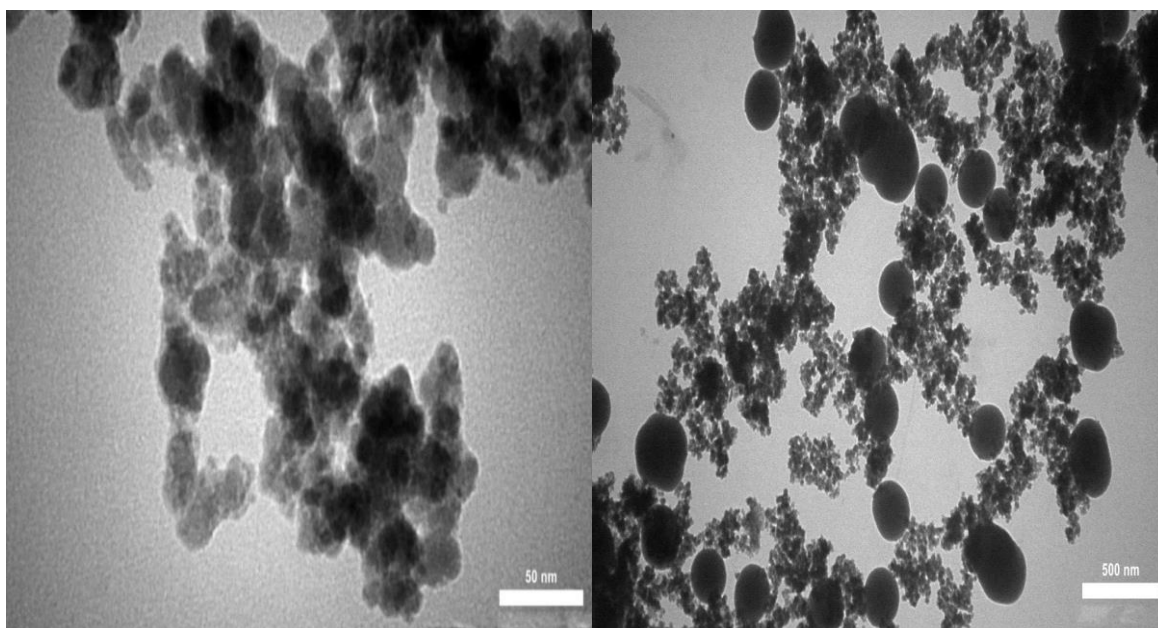
Figure 4-12: TEM picture of P2

4.3   Batch Adsorption Process

This section talks about the batch adsorption process and the factors that influencing it. An initial trial was conducted to evaluate the individual adsorption performance of the four composites (Fe_3O_4, $Fe_3O_4@SiO_2$, P1, and P2). The experimental conditions were as follows; cadmium concentration of 50 ppm, catalyst mass of 0.01 g, and duration of 30 minutes. The outcomes of this trial are presented in Table 4-3.

Table 4-3: Equilibrium concentration, removal efficiency and capacity for cadmium metal ions for the initial trial

Catalyst	C_e (ppm)	R%	q_e (mg/g)
Fe_3O_4	15.5	69	313.6
$Fe_3O_4@SiO_2$	14.1	71.8	326.3
P1	13.1	73.8	335.4
P2	13.7	72.6	330.0

4.3.1 Effect of Contact Time

Adsorption experiments were performed with differing contact time for both of composites P1 and P2 for the reason that time has a major effect on the adsorption of cadmium ions from aqueous solution. For the first composite (P1) , the adsorption experiment was carried out at room temperature using (100 ml) of aqueous solution that contains a concentration of (100 ppm) of stock solution , (0.3 g) catalyst , natural pH value (with no additives). A high removal efficiency of 94.9% was obtained during a time of 180 minutes (3 hours), after a time of 405 minutes a maximum removal of cadmium ions of 97.5% was obtained. Table 4-4 shows the removal efficiency for cadmium metal ions, and Figure 4-13 shows the variation in the

percentage removal of cadmium with contact time. The percentage of removal gradually increased over time to reach the highest value 97.5% . While for the second composite (P2) it was done under the same conditions as the first experiment in terms of concentration, mass catalyst , pH and also at the same time gradient (5-405 minutes). The results of the experiment can be seen in a Table 4-4and Figure 4-13. The highest percentage removal value reaches 91.8%.

Table 4-4: Equilibrium concentration, removal efficiency and capacity for cadmium metal ions for P1 and P2

Time(min)	P1			P2		
	C_e (ppm)	R%	q_e(mg/g)	C_e (ppm)	R%	q_e(mg/g)
5	10.2	89.8	29.933	18	82.0	27.333
15	10.1	89.9	29.967	17.4	82.6	27.533
30	9.8	90.2	30.067	15.1	84.9	28.3
45	6.9	93.1	31.033	12.3	87.7	29.233
90	6.5	93.3	31.167	11.4	88.6	29.533
180	5.1	94.9	31.633	10.6	89.4	29.8
270	4.1	95.9	31.967	9.4	90.6	30.2
360	3.0	97.0	32.333	8.6	91.4	30.467
405	2.5	97.5	32.5	8.2	91.8	30.6
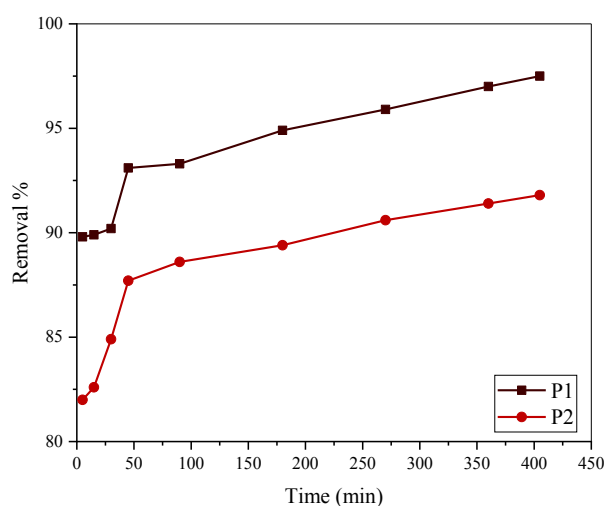
Figure 4-13: The effect of contact time on the percentage removal of cadmium for both P1 and P2

4.3.2 Effect of Concentration

By varying the initial metal ion concentrations from 25 ppm to 150 ppm in the presence of 0.3 g of catalyst, the effect of initial concentration of cadmium ion removal on P1 and P2 was studied. Figure 4-14 shows that after 405 minutes the maximum removal percentage of cadmium ions was achieved at concentration 25 ppm, which equals 99.7 for P1 and 99.3 for P2. Because there are more active sites for Cd^{+2} ions to be adsorbed on the surface of both of P1 and P2 catalysts at lower concentrations. but the effectiveness of removal gradually reduces as contaminant ion concentration increases. **(Kanrar *et al.*, 2016)** (The conditions were as follows: catalyst dosage = 0.3 g/ml, reaction time = 405 min, pH = 8). Table 4-5 illustrate equilibrium concentration, removal efficiency and capacity by varying concentrations for cadmium metal ions for P1 and P2.

Figure 4-14: The effect of concentration on the percentage removal of cadmium for both P1 and P2

Table 4-5: Equilibrium concentration, removal efficiency and capacity for cadmium metal ions for P1 and P2

Conc. (ppm)	P1			P2		
	C_e (ppm)	R%	q_e(mg/g)	C_e (ppm)	R%	q_e(mg/g)
25	0.25	99.73	8.25	0.63	99.37	8.12333
50	0.27	99.03	16.57667	1.15	98.85	16.2833
75	1.75	98.25	24.41667	3.2	96.8	23.9333
100	2.5	97.5	32.5	8.6	91.4	30.4667
125	3.1	96.9	40.63333	11.1	88.9	37.9667
150	3.8	96.2	48.73333	14.3	85.7	45.2333

4.3.3 Effect of Catalyst Dose

Figure 4-15 depicts the results of an investigation into the effect of adsorbent dose on the removal of Cd (II) ions with initial concentrations of 100 ppm, reaction time of 405 minutes, and pH of 8. The adsorption of Cd (II) increases when the quantity of adsorbent is steadily raised from 0.05g to 0.3g, leading to enhanced adsorption sites **(Murphy *et al.*, 2023)**. Experiments were carried out for both nanocomposites P1 and P2 by varying the quantity of catalyst under same conditions. The maximum adsorption occurs at an adsorbent dosage of 0.3g, with the highest removal efficiency for P1 and P2 of 97.5 and 91.8 respectively. Table 4-6 illustrate equilibrium concentration and removal efficiency by varying dose catalyst for cadmium metal ions for P1 and P2.
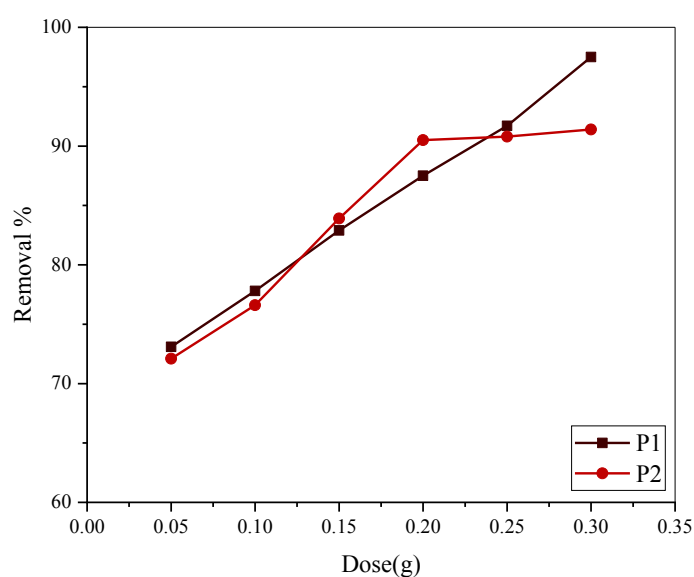
Figure 4-15: The effect of catalyst dose on the percentage removal of cadmium for both P1 and P2

Table 4-6 : Equilibrium concentration, removal efficiency and capacity by varying dose catalyst for cadmium metal ions for P1 and P2

Dose (g)	P1			P2		
	C_e (ppm)	R%	q_e(mg/g)	C_e (ppm)	R%	q_e(mg/g)
0.05	27.9	72.1	144.2	29.6	70.4	140.8
0.1	22.2	77.8	77.8	23.4	76.6	76.6
0.15	17.1	82.9	55.267	16.1	83.9	55.33
0.2	12.5	87.5	43.75	9.5	90.5	45.25
0.25	8.3	91.7	36.68	9.2	90.8	36.32
0.3	2.5	97.5	32.5	8.6	91.8	30.467

4.3.4 Effect of pH

The effect of pH was evaluated in an interval of 2.5 to 12 at 100 ppm of Cd (II), 0.3g of adsorbent for 405 minutes at room temperature. The adsorption effectiveness of Cd(II) by P2 composite is decreased when the pH value is low, as shown in Figure 4-16. When the pH is about 8, the adsorption capacity is at its peak. The adsorption effectiveness rapidly declines when the pH value rises over 8. For P1, the adsorption effectiveness increases steadily with increasing pH until it reaches its maximum efficiency at pH=10, after that point, it begins gradually drop. As an explanation for this; when the pH of the solution is low, too much H^+ causes the amino and carboxyl groups in the composites to generate $NH3^+$ and COOH, which decreases its chelating capability with Cd(II) **(Salomäki *et al.*, 2018)**. However, when the pH is too high, OH^- in aqueous solution easily hydrolyzes with Cd(II), resulting in precipitation. Table 4-7 clarify equilibrium concentration and removal efficiency by varying pH for cadmium ions for P1 and P2.
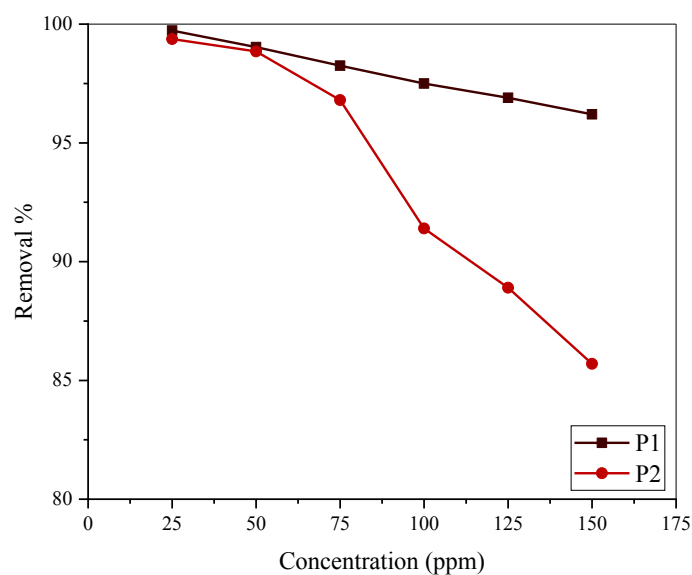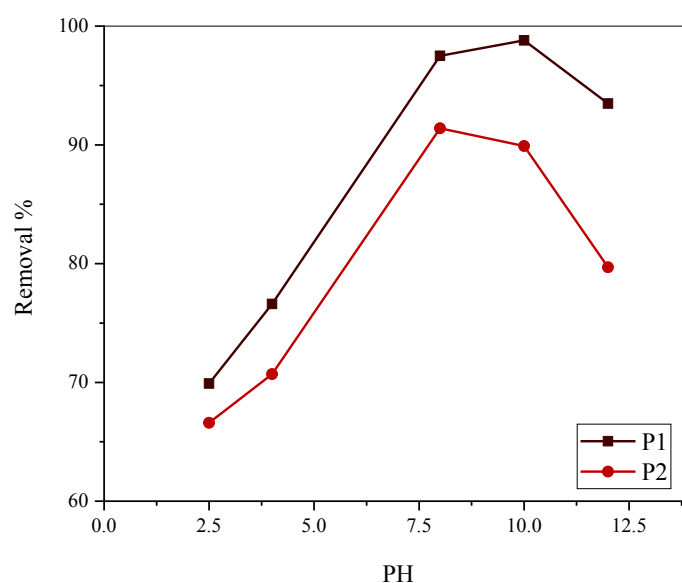
Figure 4-16: The effect of pH on the percentage removal of cadmium for both P1 and P2

Table 4-7: Equilibrium concentration, removal efficiency and capacity by varying pH for Cd(II) ions for P1 and P2

pH	P1			P2		
	C_e (ppm)	R%	q_e(mg/g)	C_e (ppm)	R%	q_e(mg/g)
2.5	30.1	69.9	23.3	33.4	66.6	22.2
4	23.4	76.6	25.533	29.3	70.7	23.567
8	2.5	97.5	32.5	8.2	91.8	30.6
10	1.2	98.8	32.933	10.1	89.9	29.967
12	6.52	93.4	31.16	20.3	79.7	26.567

4.4 Continuous Adsorption (Fixed Bed Experiments)

4.4.1 Effect of Bed Height

Three bed heights were studied (1, 1.5, and 2 cm) so as to evaluate their influence on the breakthrough curves and breakpoint at room temperature by setting the initial concentration (100 ppm), constant flow rate (5 ml/min), and pH=8. C_e/C_o values were plotted against time. Figure 4-17 shows the optimal uptake of 99% was achieved at a bed height of 1 cm. As the bed height decreases from 2 to 1cm, the breakthrough curve slightly sharpens, leading to quicker saturation and consequently, fastest saturation. Conversely, the slope of the breakthrough curve was reduced by increasing the bed from 1.5 to 2 cm height due to the expansion of the mass-transfer zone **(Thirunavukkarasu, Nithya and Sivashankar, 2021)**. This result in achieving higher breakthrough points and improved overall efficiency. Results obtain from continuous adsorption are shown in Table 1, Appendix B.
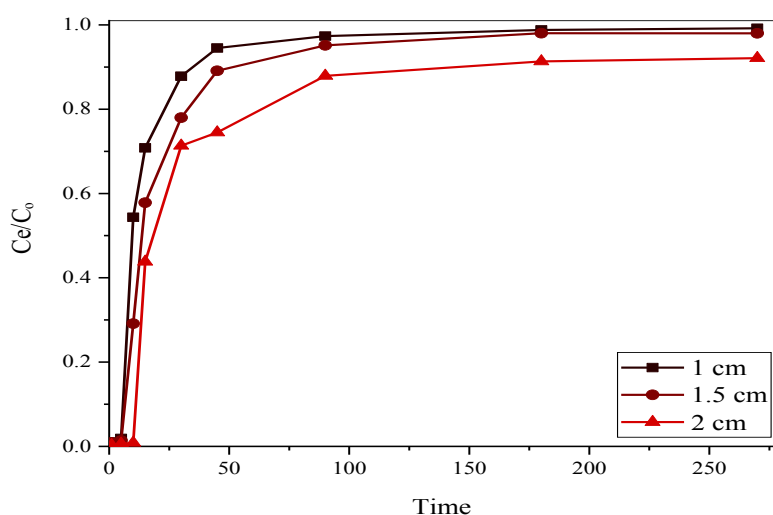
Figure 4-17: Breakthrough curves for adsorption of Cd (II) onto Fe$_3$O$_4$@SiO$_2$/P(AANa-co-PABA) at pH 8 and 100 ppm and Q=5 ml/min

4.4.2 Effect of Initial Concentration

Experiments were carried out at room temperature with varied initial concentrations (50, 100, and 150 ppm) at room temperature, with bed height at 1 cm and flow rate of 5 mL/min. As observed in Figure 4-18, and Table 2 in Appendix B, the beds experienced faster breakthrough at higher initial concentrations. As the adsorption sites in the column became rapidly saturated, the breakpoint time decreased with increasing initial concentration of the adsorbate. On the other hand, a reduction in initial concentration resulted in an expanded breakthrough curve, suggesting that a larger volume of solution could be treated. This phenomenon can be attributed to the lower concentration gradient, which induces slower transport due to a decrease in diffusion or mass transfer coefficient **(Fallah and Taghizadeh, 2020) (Ahmad and Hameed, 2010)**.
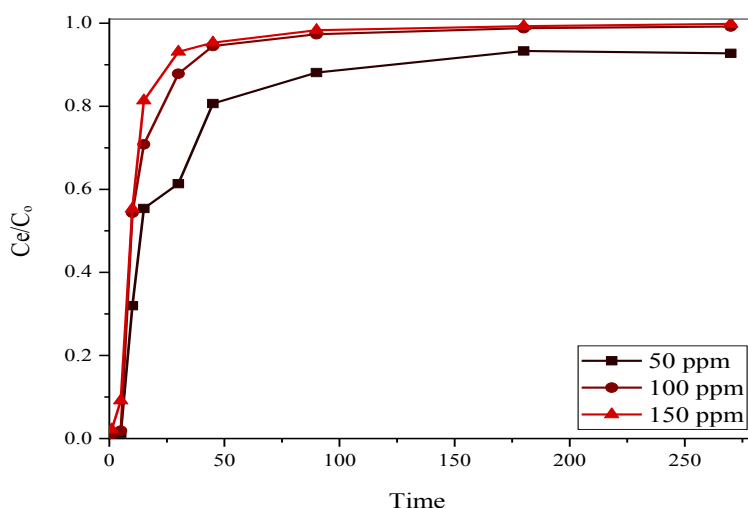
Figure 4-18: Breakthrough curves for adsorption of Cd (II) onto P1 at pH 8 and 1cm bed height and Q=5 ml/min

4.4.3 Effect of the Solution Flowrate

The effect of flow rate on Cd(II) adsorption was studied by adjusting the flow rate (5 and 10 mL/min) with a constant adsorbent bed height of 1cm and an initial concentration of 100 ppm, as shown in Figure 4-19 and Table 3 in Appendix B. It was found that increased flow rates resulted in speedier breakthrough. The change in the slope of the breakthrough curve may be explained using mass transfer principles. The reason for this is because as flow rate increases, so does the rate of mass transfer, for example the quantity of Cd^{+2} adsorbed onto unit bed height (mass transfer zone), resulting in more quickly saturation at higher flow rate **(Ahmad and Hameed, 2010)**.
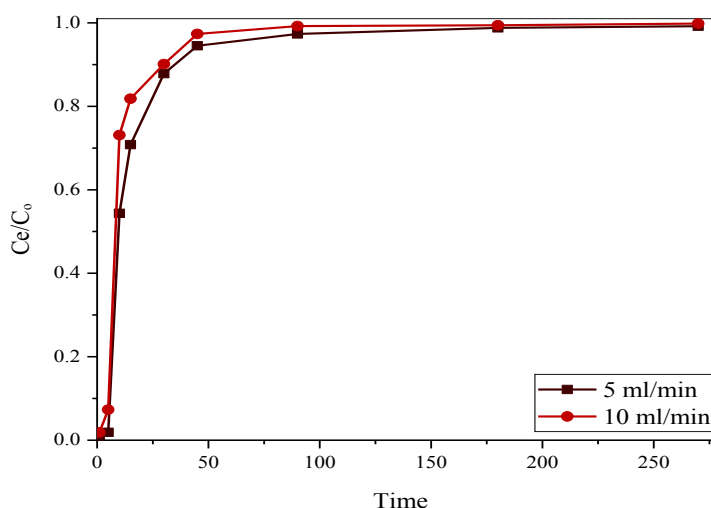
Figure 4-19: Breakthrough curves for adsorption of Cd (II) onto P1at pH 8 and 1cm bed height and 100 ppm

4.5 Adsorption Isotherms

Heavy metal adsorption isotherms were employed for P1 and P2 in batch experiments at pH neutral, adsorbent quantity 0.3g and varying metal concentration from 25-150 ppm.

The results proved that for P1 the Freundlich isotherm model indicated by the highest R^2 of 0.98 when compared to Langmuir model (R^2=0.95) and Temkin model (R^2=0.83). This model postulates that the concentration of adsorbate on the adsorbent surface rises alongside the adsorbate concentration, potentially resulting in infinite adsorbed quantities. The value of (n=1.5) characterizes a heterogeneous distribution of surface sites magnetic nanoparticle surface, leading the Cd (II) ions to occupy most strong sites first forming multi-layered **(Danesh, Ghorbani and Marjani, 2021)**. Figures 4-20 to 4-22 shows P1 isotherms. Table 4-8 shows the parameters and correlation coefficient for P1. While for P2 the results revealed fitting with Langmuir isotherm model (R^2=0.96) better than the other two models. This indicates monolayer adsorption on a homogeneous surface, with a finite number of identical sites available for adsorption, and a uniform adsorption strategy by the adsorbent to prevent migration on a flat surface **(Leiva, Tapia and Rodríguez, 2021)**. Figures 4-23 to 4-25 depict P2 isotherms, with corresponding parameters and correlation coefficients in Table 4-9. K_L, the Langmuir adsorption constant, characterizes the equilibrium between adsorbed molecules and vacant adsorption sites. R_L, a dimensionless separation factor, indicates adsorption favorability: $0 < R_L < 1$ signifies favorability, $R_L = 1$ implies linearity, and $R_L > 1$ suggests an unfavorable process.
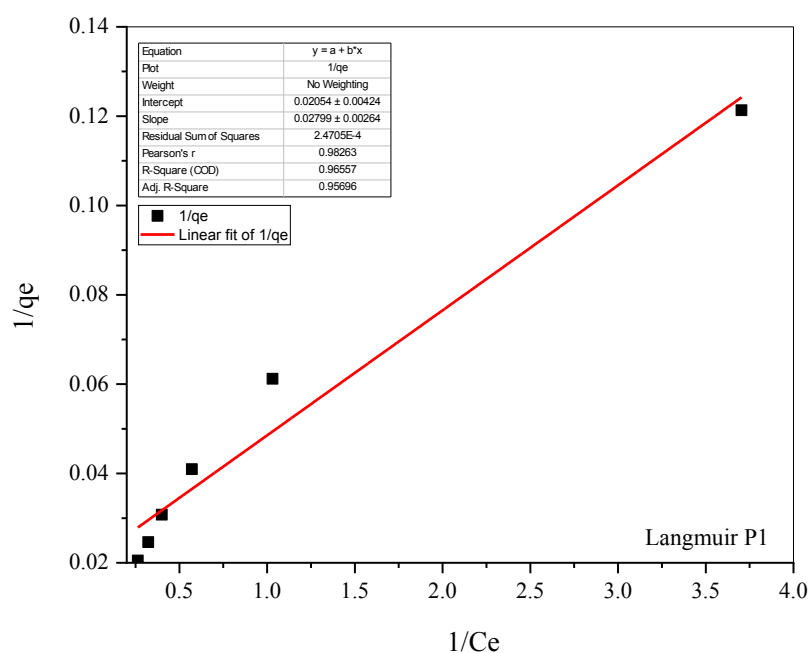
Figure 4-20: A fit of Cd(II) adsorption to Langmuir model using P1 at 100 ppm
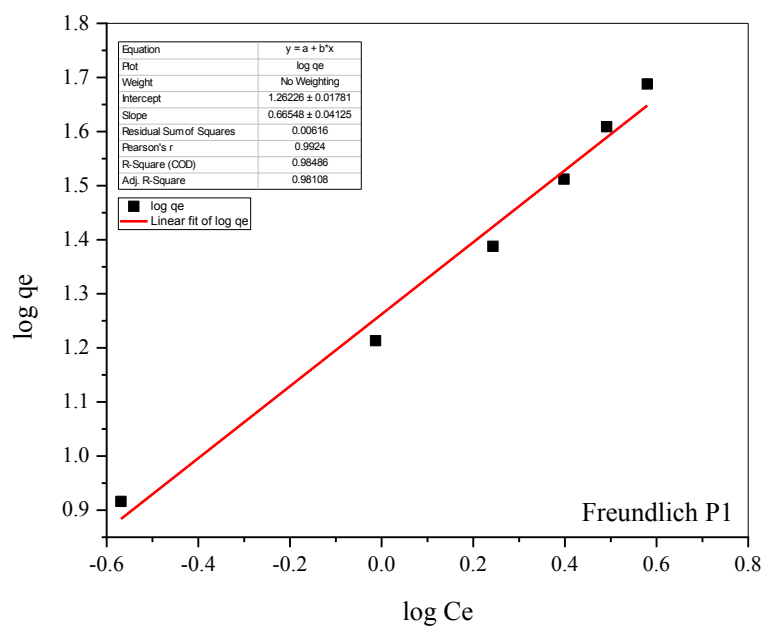
Figure 4-21: A fit of Cd(II) adsorption to Freundlich model using P1 at 100 ppm
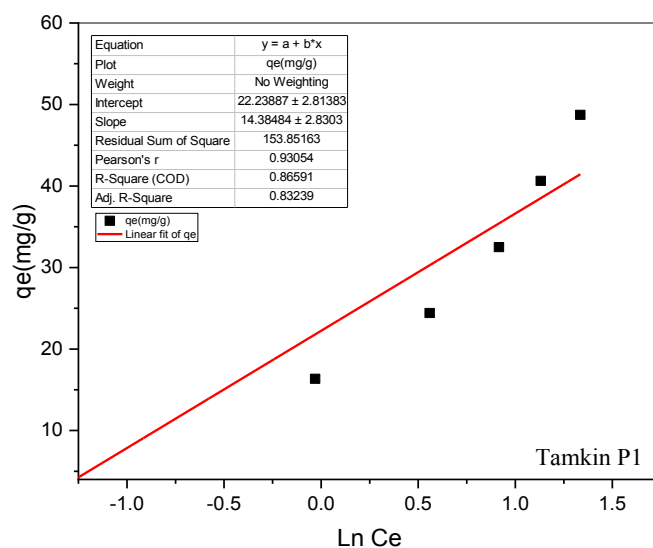
Figure 4-22: A fit of Cd(II) adsorption to Tamkin model using P1 at 100 ppm

Table 4-8: parameters and correlation coefficient (R^2) for each isotherm model for the P1 composite at 100 ppm concentration of Cd (II) and 0.3g catalyst

Isotherms	Parameters		
Langmuir	K_L	R_L	R^2
	0.73383351	0.01344387	0.95696
Freundlich	1/n	K_F	R^2
	0.66548	18.2919498	0.98108
Tamkin	B_T	K_T	R^2
	14.38484	4.69263172	0.83239

Equation	y = a + b*x
Plot	1/qe
Weight	No Weighting
Intercept	0.02005 ± 0.00405
Slope	0.06133 ± 0.00538
Residual Sum of Squares	2.14434E-4
Pearson's r	0.98493
R-Square (COD)	0.97009
Adj. R-Square	0.96262
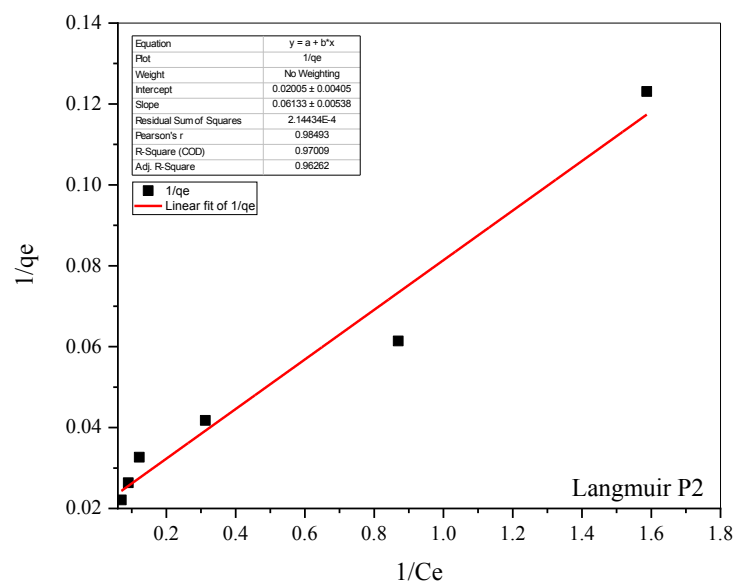
Figure 4-23: A fit of Cd(II) adsorption to Langmuir model using P2 at 100 ppm

Equation	y = a + b*x
Plot	log qe
Weight	No Weighting
Intercept	1.09174 ± 0.04372
Slope	0.4801 ± 0.05674
Residual Sum of Squares	0.01988
Pearson's r	0.97318
R-Square (COD)	0.94708
Adj. R-Square	0.93385
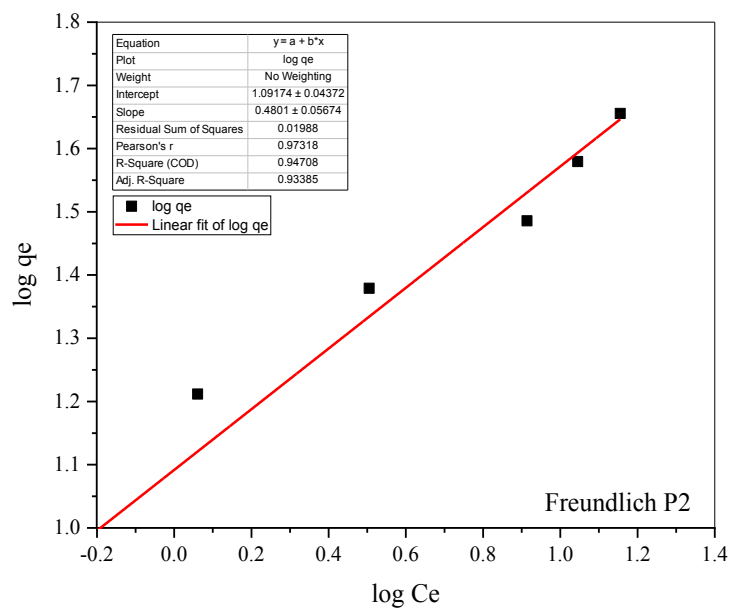
Figure 4-24: A fit of Cd(II) adsorption to Freundlich model using P2 at 100 ppm

Equation	y = a + b*x
Plot	qe
Weight	No Weighting
Intercept	13.0003 ± 2.05003
Slope	10.50124 ± 1.15556
Residual Sum of Squares	43.71536
Pearson's r	0.97663
R-Square (COD)	0.9538
Adj. R-Square	0.94225
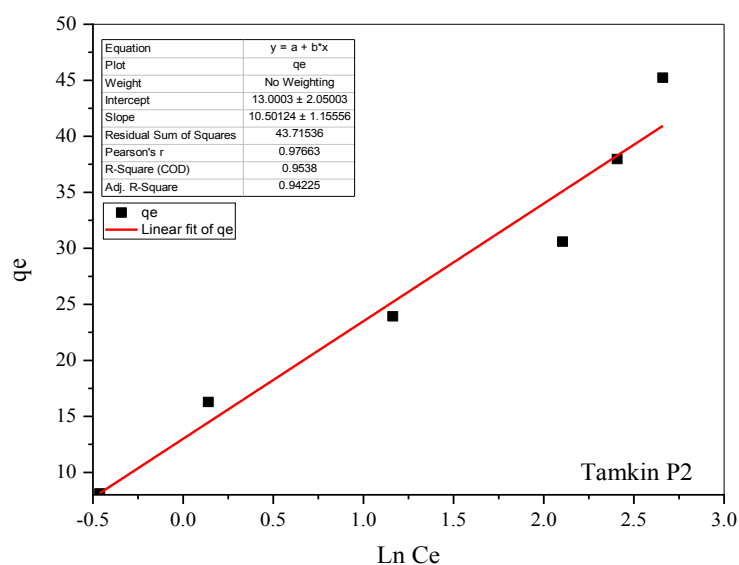
Tamkin P2

Figure 4-25: A fit of Cd(II) adsorption to Tamkin model using P2 at 100 ppm

Table 4-9: Parameters and correlation coefficient (R^2) for each isotherm model for the P2 composite at 100 ppm concentration of Cd (II) and 0.3g catalyst

Isotherms	Parameters		
Langmuir	K_L	R_L	R^2
	0.3269199	0.0296806	0.96262
Freundlich	1/n	K_F	R^2
	0.4801	12.352077	0.93385
Tamkin	B_T	K_T	R^2
	10.50124	3.448632	0.94225

4.6   Kinetic Adsorption

The kinetics of cadmium adsorption on adsorbent materials P1 and P2 play a major role in identifying the most suitable operating parameters for batch adsorption and describe the mechanism of aqueous solute sorption onto an adsorbent. Adsorption kinetics study defines the capacity of the uptake rate to influence the residence time spent by the adsorbate at the solution interface. Cadmium adsorption kinetic data can be well fitted to the pseudo-second-order kinetics model for both P1 and P2 composites with almost perfect correlation coefficient of 0.99, while poor fittings were generated if the pseudo-first-order model was used (the kinetic parameters are shown in Tables 4-10 and 4-11). This indicates that adsorption of cadmium onto adsorbent may be the chemisorption involving valence forces through exchange or sharing of electrons between nano-sized metal oxide and cadmium **(Kumar and Chawla, 2014)**. Figures 4-26 to 4-29 depict the use of the pseudo-first-order and pseudo-second-order model on the P1 and P2 respectively at 100 ppm cadmium concentration and 0.3 g mass of catalyst.

1st P1

Equation	y = a + b*x
Plot	Ln(qe-qt)
Weight	No Weighting
Intercept	1.05771 ± 0.11356
Slope	-0.00819 ± 5.31944
Residual Sum of Squar	0.38114
Pearson's r	-0.98554
R-Square (COD)	0.97129
Adj. R-Square	0.96718
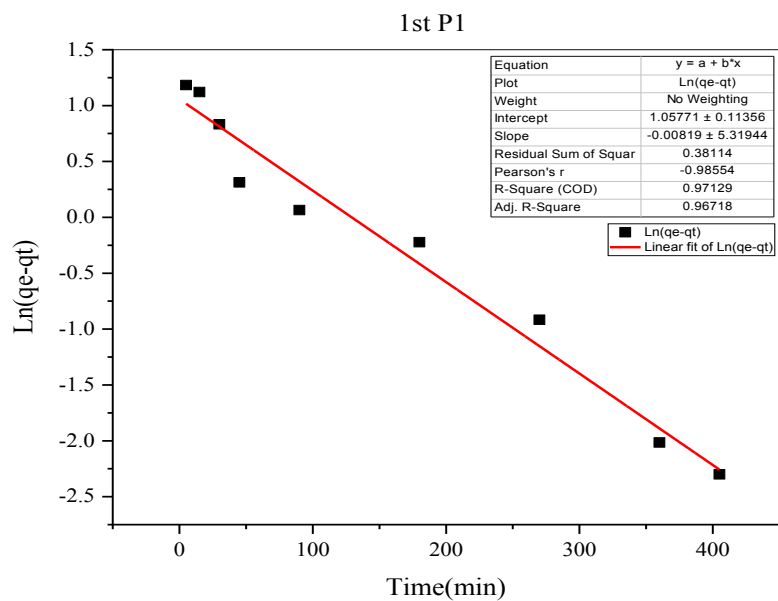
Figure 4-26: Pseudo-first-order kinetic plot for Cd(II) adsorption by P1 nanocomposite at concentration 100 ppm

2nd P1

Equation	y = a + b*x
Plot	t/qt
Weight	No Weighting
Intercept	0.07363 ± 0.02786
Slope	0.03077 ± 1.30512E
Residual Sum of Squar	0.02294
Pearson's r	0.99994
R-Square (COD)	0.99987
Adj. R-Square	0.99986
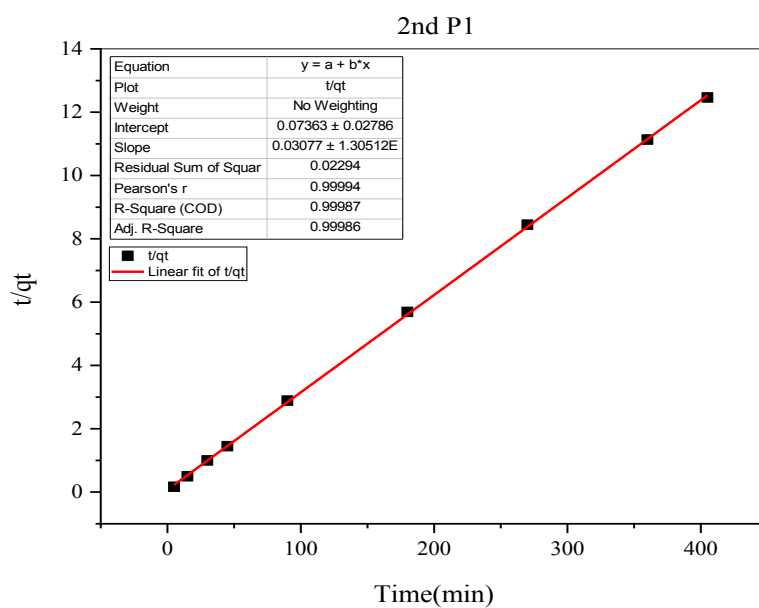
Figure 4-27: Pseudo-second-order kinetic plot for Cd(II) adsorption by P1 nanocomposite at concentration 100 ppm

1st P2

Equation	y = a + b*x
Plot	Ln(qe-qt)
Weight	No Weighting
Intercept	1.05771 ± 0.11356
Slope	-0.00819 ± 5.31944E
Residual Sum of Squar	0.38114
Pearson's r	-0.98554
R-Square (COD)	0.97129
Adj. R-Square	0.96718
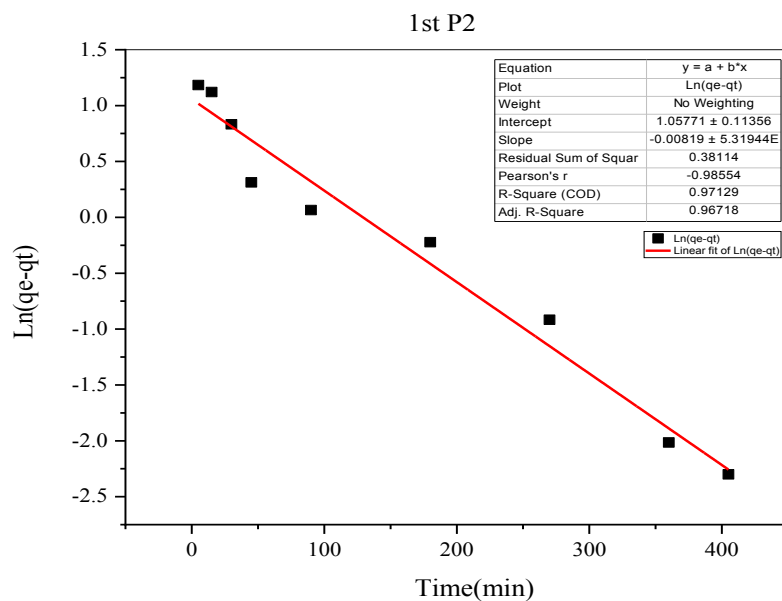
Figure 4-28: Pseudo-first-order kinetic plot for Cd(II) adsorption by P2 nanocomposite at concentration 100 ppm

2nd P2

Equation	y = a + b*x
Plot	t/qt
Weight	No Weighting
Intercept	0.07878 ± 0.02536
Slope	0.03264 ± 1.18783E-
Residual Sum of Square	0.019
Pearson's r	0.99995
R-Square (COD)	0.99991
Adj. R-Square	0.99989
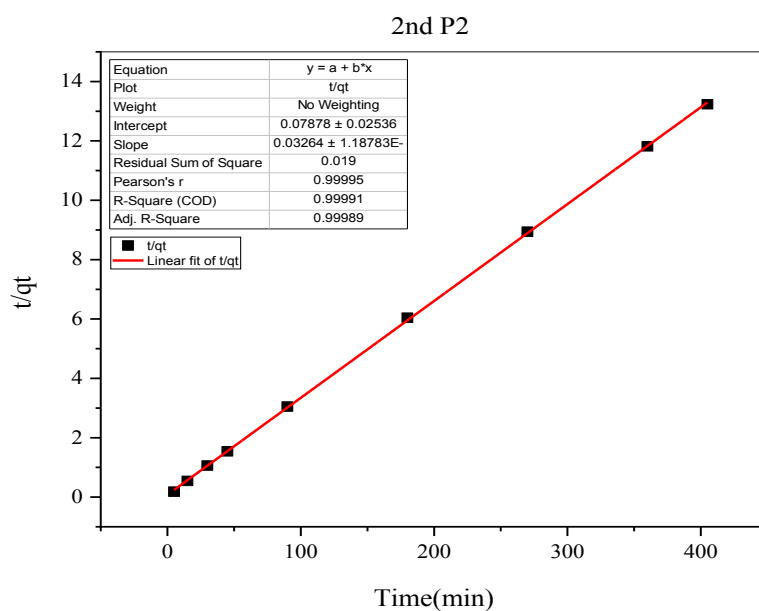
Figure 4-29: Pseudo-second-order kinetic plot for Cd(II) adsorption by P2 nanocomposite at concentration 100 ppm

Table 4-10: parameters and correlation coefficient (R^2) for each kinetic model [0.3g of P1 at 100ppm concentration for Cd (II)]

Pseudo-first-order constants		
q_e (mg/g)	k_1 (min^{-1})	R^2
2.87977	-2.02222E-05	0.96718
Pseudo-second-order constants		
q_e (mg/g)	K_2 (min^{-1})	R^2
32.4992	0.01286	0.99986

Table 4-11 : parameters and correlation coefficient (R^2) for each kinetic model [0.3g of P2 at 100ppm concentration for Cd (II)]

Pseudo-first-order constants		
q_e (mg/g)	k_1 (min^{-1})	R^2
2.87977	-2.02222E-05	0.96718
Pseudo-second-order constants		
q_e (mg/g)	K_2 (min^{-1})	R^2
30.6373	0.01352	0.99989

CHAPTER 5

CONCLUSIONS AND RECOMMENDATIONS

5.1 Conclusions

1. Two nanocomposites adsorbent were efficiently synthesized in this work.

2. The composites exhibits good magnetic responsiveness, which give it high potential to remove Cd(II) from wastewater.

3. For adsorption experiments, the efficiency of removal decreases as heavy metal concentration increase and the increase in the amount of adsorbents leads to an increase in removal efficiency as a result of the more available active site. The optimal pH solution was achieved at a neutral level.

4. The adsorption isotherm fitted well with Frendlich isotherm rather than Langmuir for P1, while for P2,The Langmuir isotherm shows best result.

5. The adsorption kinetics study of Cd(II) on the magnetic composites can be well described by the pseudo-second-order model.

6. the adsorption capacity values were 335.4 and 330.0 mg/g for P1 and P2 respectively (initial concentration 50 mg/L) and (adsorbent amount 0.011g) for (30 min).

5.2   Recommendations for Future Work

As a result of these findings, it is recommended that:

1. Other acids can be used as copolymers and their effectiveness can be explored.
2. Study the effect of temperature and shaking speed on adsorption efficiency.
3. Try another type of heavy metals as pollutants.

REFERENCES

Aarab, N. et al. (2020) 'Removal of an emerging pharmaceutical pollutant (metronidazole) using PPY-PANi copolymer: kinetics, equilibrium and DFT identification of adsorption mechanism', Groundwater for Sustainable Development, 11, p. 100416.

Ahmad, A.A. and Hameed, B.H. (2010) 'Fixed-bed adsorption of reactive azo dye onto granular activated carbon prepared from waste', Journal of hazardous materials, 175(1–3), pp. 298–303.

Ali, H. and Khan, E. (2018) 'What are heavy metals? Long-standing controversy over the scientific use of the term "heavy metals"–proposal of a comprehensive definition', Toxicological & Environmental Chemistry, 100(1), pp. 6–19.

Alka, S. et al. (2021) 'Arsenic removal technologies and future trends: A mini review', Journal of cleaner production, 278, p. 123805.

Alterary, S.S. and AlKhamees, A. (2021) 'Synthesis, surface modification, and characterization of Fe3O4@ SiO2 core@ shell nanostructure', Green Processing and Synthesis, 10(1), pp. 384–391.

Aoshima, K. (2016) 'Itai-itai disease: Renal tubular osteomalacia induced by environmental exposure to cadmium—historical review and perspectives', Soil Science and Plant Nutrition, 62(4), pp. 319–326.

Ben-Ali, S. et al. (2017) 'Characterization and adsorption capacity of raw pomegranate peel biosorbent for copper removal', Journal of cleaner production, 142, pp. 3809–3821.

Bilal, M. et al. (2021) 'Recent advances in applications of low-cost adsorbents

References

for the removal of heavy metals from water: A critical review', Separation and Purification Technology, 278, p. 119510.

Boruah, P.K. et al. (2015) 'Facile synthesis and characterization of Fe3O4 nanopowder and Fe3O4/reduced graphene oxide nanocomposite for methyl blue adsorption: a comparative study', Journal of Environmental Chemical Engineering, 3(3), pp. 1974–1985.

Çelebi, H., Gök, G. and Gök, O. (2020) 'Adsorption capability of brewed tea waste in waters containing toxic lead (II), cadmium (II), nickel (II), and zinc (II) heavy metal ions', Scientific reports, 10(1), p. 17570.

Christy, E.J.S. et al. (2023) 'Development of nanorods-like Fe2O3@ functionalized carboxy methyl cellulose–SiO2 composite for the removal of pesticides and antibiotics', Environmental Nanotechnology, Monitoring & Management, 20, p. 100834.

Da'na, E. and Sayari, A. (2012) 'Adsorption of heavy metals on amine-functionalized SBA-15 prepared by co-condensation: Applications to real water samples', Desalination, 285, pp. 62–67.

Danesh, N., Ghorbani, M. and Marjani, A. (2021) 'Separation of copper ions by nanocomposites using adsorption process', Scientific Reports, 11(1), pp. 1–23.

Dehghani, M.H. et al. (2018) 'Adsorptive removal of noxious cadmium from aqueous solutions using poly urea-formaldehyde: a novel polymer adsorbent', MethodsX, 5, pp. 1148–1155.

Dhawane, S.H., Kumar, T. and Halder, G. (2016) 'Parametric effects and optimization on synthesis of iron (II) doped carbonaceous catalyst for the production of biodiesel', Energy Conversion and Management, 122, pp. 310–

References

320.

Emrani, S. et al. (2023) 'Magnetic fibrous silica mesoporous as a selective and efficient system for removal of Cd (II) ions with a focus on optimization by response surface methodology', International Journal of Environmental Analytical Chemistry, 103(4), pp. 849–867.

Fakirov, S. (2018) 'Nanofibrillar polymer–polymer and single polymer composites via the "converting instead of adding" concept–examples of true polymer nanocomposite', Advanced Industrial and Engineering Polymer Research, 1(1), pp. 40–47.

Fallah, N. and Taghizadeh, M. (2020) 'Continuous fixed-bed adsorption of Mo (VI) from aqueous solutions by Mo (VI)-IIP: Breakthrough curves analysis and mathematical modeling', Journal of Environmental Chemical Engineering, 8(5), p. 104079.

Fan, F.-L. et al. (2012) 'Rapid removal of uranium from aqueous solutions using magnetic Fe3O4@ SiO2 composite particles', Journal of environmental radioactivity, 106, pp. 40–46.

Georgieva, V.G. et al. (2015) 'Adsorption kinetics of Cr (VI) ions from aqueous solutions onto black rice husk ash', Journal of Molecular Liquids, 208, pp. 219–226.

Goyal, R.K. (2017) Nanomaterials and nanocomposites: synthesis, properties, characterization techniques, and applications. CRC Press.

Guarín-Romero, J.R. et al. (2019) 'Simple and competitive adsorption study of nickel (II) and chromium (III) on the surface of the brown algae Durvillaea antarctica biomass', ACS omega, 4(19), pp. 18147–18158.

References

Guleria, A., Kumari, G. and Lima, E.C. (2020) 'Cellulose-g-poly-(acrylamide-co-acrylic acid) polymeric bioadsorbent for the removal of toxic inorganic pollutants from wastewaters', Carbohydrate polymers, 228, p. 115396.

Hazra, B. et al. (2018) 'Porosity controls and fractal disposition of organic-rich Permian shales using low-pressure adsorption techniques', Fuel, 220, pp. 837–848.

He, S. et al. (2016) 'Synthesis of sodium acrylate and acrylamide copolymer/GO hydrogels and their effective adsorption for Pb2+ and Cd2+', ACS Sustainable Chemistry & Engineering, 4(7), pp. 3948–3959.

Hua, R. and Li, Z. (2014) 'Sulfhydryl functionalized hydrogel with magnetism: Synthesis, characterization, and adsorption behavior study for heavy metal removal', Chemical Engineering Journal, 249, pp. 189–200.

Hussain, A., Madan, S. and Madan, R. (2021) 'Removal of heavy metals from wastewater by adsorption', Heavy Metals—Their Environmental Impacts and Mitigation [Preprint].

Kanrar, S. et al. (2016) 'Preparation, characterization and evaluation of fluoride adsorption efficiency from water of iron-aluminium oxide-graphene oxide composite material', Chemical Engineering Journal, 306, pp. 269–279.

Khalid, K. et al. (2020) 'Advanced in developmental organic and inorganic nanomaterial: A review', Bioengineered, 11(1), pp. 328–355.

Khulbe, K.C. and Matsuura, T. (2018) 'Removal of heavy metals and pollutants by membrane adsorption techniques', Applied Water Science, 8(1). Available at: https://doi.org/10.1007/s13201-018-0661-6.

References

Koo, J.H. (2019) Polymer nanocomposites: processing, characterization, and applications. McGraw-Hill Education.

Kumar, R. and Chawla, J. (2014) 'Removal of cadmium ion from water/wastewater by nano-metal oxides: a review', Water Quality, Exposure and Health, 5, pp. 215–226.

Kumar, S., Supriya, S. and Kar, M. (2018) 'Enhancement of dielectric constant in polymer-ceramic nanocomposite for flexible electronics and energy storage applications', Composites Science and Technology, 157, pp. 48–56.

Leiva, E., Tapia, C. and Rodríguez, C. (2021) 'Removal of Mn (II) from Acidic Wastewaters Using Graphene Oxide–ZnO Nanocomposites', Molecules, 26(9), p. 2713.

Liu, H., Wang, Q. and Zhang, F. (2020) 'Preparation of Fe3O4@ SiO2@ P (AANa-co-AM) composites and their adsorption for Pb (II)', ACS omega, 5(15), pp. 8816–8824.

Liu, K. et al. (2020) 'Simultaneous removal of Cd (II) and As (III) by graphene-like biochar-supported zero-valent iron from irrigation waters under aerobic conditions: Synergistic effects and mechanisms', Journal of Hazardous Materials, 395, p. 122623.

Liu, L. and Corma, A. (2018) 'Metal catalysts for heterogeneous catalysis: from single atoms to nanoclusters and nanoparticles', Chemical reviews, 118(10), pp. 4981–5079.

Liu, T. et al. (2019) 'Tailor-made core/shell/shell-like Fe3O4@ SiO2@ PPy composites with prominent microwave absorption performance', Journal of Alloys and Compounds, 779, pp. 831–843.

References

Lu, H. et al. (2016) 'An overview of nanomaterials for water and wastewater treatment', Advances in Materials Science and Engineering, 2016.

Lu, K. (2020) 'Hybrid materials–a review on co-dispersion, processing, patterning, and properties', International Materials Reviews, 65(8), pp. 463–501.

Lu, Z. et al. (2008) 'Facile synthesis of Fe3O4/SiO2 composite nanoparticles from primary silica particles', Colloids and Surfaces A: Physicochemical and Engineering Aspects, 317(1–3), pp. 450–456.

Lunge, S., Singh, S. and Sinha, A. (2014) 'Magnetic iron oxide (Fe3O4) nanoparticles from tea waste for arsenic removal', Journal of Magnetism and Magnetic Materials, 356, pp. 21–31.

Masulli, M. et al. (2022) 'Temperature effect on the dynamic adsorption of anionic surfactants and alkalis to silica surfaces', Petroleum Science, 19(4), pp. 1866–1876.

Motitswe, M.G., Badmus, K.O. and Khotseng, L. (2022) 'Development of adsorptive materials for selective removal of toxic metals in wastewater: A review', Catalysts, 12(9), p. 1057.

Mukhopadhyay, R. et al. (2020) 'Clay–polymer nanocomposites: Progress and challenges for use in sustainable water treatment', Journal of hazardous materials, 383, p. 121125.

Murphy, O.P. et al. (2023) 'A Review on the Adsorption Isotherms and Design Calculations for the Optimization of Adsorbent Mass and Contact Time', ACS omega, 8(20), pp. 17407–17430.

Nagalakshmaiah, M. et al. (2019) 'Biocomposites: Present trends and

References

challenges for the future', Green composites for automotive applications, pp. 197–215.

Nawaz, T. et al. (2020) 'Synthesis of diglycolic acid functionalized core-shell silica coated Fe3O4 nanomaterials for magnetic extraction of Pb (II) and Cr (VI) ions', Scientific Reports, 10(1), p. 10076.

Okamoto, K. and Takahashi, K. (2020) 'Ion exchange membrane, method for producing ion exchange membrane, and electrolyzer'. Google Patents.

Revellame, E.D. et al. (2020) 'Adsorption kinetic modeling using pseudo-first order and pseudo-second order rate laws: A review', Cleaner Engineering and Technology, 1, p. 100032.

Saha, N. et al. (2016) 'Spatial distribution and contamination assessment of six heavy metals in soils and their transfer into mature tobacco plants in Kushtia District, Bangladesh', Environmental Science and Pollution Research, 23, pp. 3414–3426.

Saha, N. et al. (2017) 'Industrial metal pollution in water and probabilistic assessment of human health risk', Journal of environmental management, 185, pp. 70–78.

Salomäki, M. et al. (2018) 'Effects of pH and oxidants on the first steps of polydopamine formation: a thermodynamic approach', The Journal of Physical Chemistry B, 122(24), pp. 6314–6327.

Sarkar, A., Ravindran, G. and Krishnamurthy, V. (2013) 'A brief review on the effect of cadmium toxicity: from cellular to organ level', Int J Biotechnol Res, 3(1), pp. 17–36.

Sen, T. and Khoo, C. (2013) 'Adsorption characteristics of zinc (Zn2+) from

References

aqueous solution by natural bentonite and kaolin clay minerals: a comparative study', Computational Water, Energy, and Environmental Engineering, 2, pp. 1–6.

Sharma, G. and Naushad, M. (2020) 'Adsorptive removal of noxious cadmium ions from aqueous medium using activated carbon/zirconium oxide composite: Isotherm and kinetic modelling', Journal of Molecular Liquids, 310, p. 113025.

Sharma, M. et al. (2023) 'Sequestration and recovery of thorium ions using a recyclable, low-cost, glutathione-based magnetic nanocomposite: experimental study and statistical modeling', Separation and Purification Technology, p. 124264.

Sharma, S. and Bhattacharya, A. (2017) 'Drinking water contamination and treatment techniques', Applied water science, 7(3), pp. 1043–1067.

Shrestha, R. et al. (2021) 'Technological trends in heavy metals removal from industrial wastewater: A review', Journal of Environmental Chemical Engineering, 9(4), p. 105688.

Singh, V. et al. (2023) 'Adsorption Studies of Pb (II) and Cd (II) Heavy Metal Ions from Aqueous Solutions Using a Magnetic Biochar Composite Material', Separations, 10(7), p. 389.

Song, Y. et al. (2019) 'Highly efficient adsorption of Pb (II) from aqueous solution using amino-functionalized SBA-15/calcium alginate microspheres as adsorbent', International journal of biological macromolecules, 125, pp. 808–819.

Stala, Ł., Ulatowska, J. and Polowczyk, I. (2021) 'A review of polyampholytic ion scavengers for toxic metal ion removal from aqueous

References

systems', Water Research, 203, p. 117523.

Sun, S., Li, H. and Xu, Z.J. (2018) 'Impact of surface area in evaluation of catalyst activity', Joule, 2(6), pp. 1024–1027.

Sun, Y. et al. (2020) 'Performance evaluation and optimization of flocculation process for removing heavy metal', Chemical Engineering Journal, 385, p. 123911.

Tao, Y. et al. (2020) 'Removal of Pb (II) ions from wastewater by using polyethyleneimine-functionalized Fe3O4 magnetic nanoparticles', Applied Sciences, 10(3), p. 948.

Thilagan, J. et al. (2015) 'Continuous fixed bed column adsorption of copper (II) ions from aqueous solution by calcium carbonate', International Journal of Engineering Research & Technology, 4(12), pp. 413–416.

Thirunavukkarasu, A., Nithya, R. and Sivashankar, R. (2021) 'Continuous fixed-bed biosorption process: A review', Chemical Engineering Journal Advances, 8, p. 100188.

Tian, Y. et al. (2023) 'Highly efficient adsorbent for removing uranium from water based on a novel phosphate esterification hyper-cross-linked polymer', Journal of Molecular Liquids, p. 122431.

Veerakumar, P. et al. (2015) 'Nickel nanoparticle-decorated porous carbons for highly active catalytic reduction of organic dyes and sensitive detection of Hg (II) ions', ACS applied materials & interfaces, 7(44), pp. 24810–24821.

Wang, J. and Guo, X. (2020) 'Adsorption isotherm models: Classification, physical meaning, application and solving method', Chemosphere, 258, p. 127279.

References

Wang, L. et al. (2023) 'Molecular imprinting-based nanocomposite adsorbents for typical pollutants removal', Journal of Hazardous Materials Letters, 4, p. 100073.

Wang, Y. et al. (2020) 'Fabrication of O-enriched hypercross-linked polymers and their adsorption of aniline from aqueous solution', Industrial & Engineering Chemistry Research, 59(25), pp. 11705–11712.

Wolska, J. et al. (2023) 'The influence of cross-linking density on the efficiency of post-synthetic sulfonation of hyper-cross-linked polymers and their adsorption capacity for antibiotic pollutants', Journal of Environmental Chemical Engineering, p. 110429.

Yao, W. et al. (2022) 'Magnetic activated carbon optimization using response surface approach for Cr (VI)', in IOP Conference Series: Earth and Environmental Science. IOP Publishing, p. 12002.

Zarei, A., Saedi, S. and Seidi, F. (2018) 'Synthesis and application of Fe3O4@ SiO2@ carboxyl-terminated PAMAM dendrimer nanocomposite for heavy metal removal', Journal of Inorganic and Organometallic Polymers and Materials, 28(6), pp. 2835–2843.

Zhang, X., He, X. and Zhao, S. (2021) 'Preparation of a novel Fe3O4@SiO2@propyl@DBU magnetic core–shell nanocatalyst for Knoevenagel reaction in aqueous medium', Green Chemistry Letters and Reviews. Taylor and Francis Ltd., pp. 83–96. Available at: https://doi.org/10.1080/17518253.2020.1862312.

Zhou, X., Maimaitiniyazi, R. and Wang, Y. (2022) 'Some consideration triggered by misquotation of Temkin model and the derivation of its correct form', Arabian Journal of Chemistry, p. 104267.

APPENDICES

APPENDIX A:

Energy Dispersive X-Ray Spectroscopy (EDX) Test

Table 1: EDX for P1

Element	Apparent Concentration	k Ratio	Wt%	Wt% Sigma	Atomic %	Factory Standard
C	0.51	0.00513	13.18	0.32	22.29	Yes
N	0.60	0.00106	2.08	0.27	3.02	Yes
O	10.78	0.03628	42.28	0.28	53.70	Yes
Na	0.01	0.00004	0.05	0.06	0.04	Yes
Si	3.33	0.02640	15.35	0.13	11.10	Yes
Fe	5.09	0.05086	27.06	0.27	9.85	Yes
Total:			100.00		100.00	

Table 2: EDX for P2

Element	Apparent Concentration	k Ratio	Wt%	Wt% Sigma	Atomic %	Factory Standard
C	0.33	0.00334	9.30	0.31	17.04	Yes
N	0.43	0.00077	1.46	0.25	2.30	Yes
O	10.39	0.03497	39.62	0.28	54.52	Yes
Na	0.30	0.00126	1.60	0.08	1.53	Yes
Si	2.98	0.02362	14.59	0.13	11.43	Yes
Fe	6.11	0.06107	33.43	0.29	13.18	Yes
Total:			100.00		100.00	

APPENDIX B:

Results obtain from continuous adsorption of Cd (II)

Table 1: Continuous adsorption at Q= 5 ml/min and 100 ppm of Cd (II)

Time (min)	Ce. Height (cm)			Ce/C_o	Ce/C_o	Ce/C_o
	1	**1.5**	**2**			
1	1.03	0.95	0.32	0.0103	0.0095	0.0032
5	1.89	1.39	0.63	0.0189	0.0139	0.0063
10	54.35	29.11	0.87	0.5435	0.2911	0.0087
15	70.81	57.81	43.81	0.7081	0.5781	0.4381
30	87.83	77.98	71.33	0.8783	0.7798	0.7133
45	94.51	89.11	74.48	0.9451	0.8911	0.7448
90	97.33	95.13	87.9	0.9733	0.9513	0.879
180	98.8	98.02	91.33	0.988	0.9802	0.9133
270	99.21	98.01	92.11	0.9921	0.9801	0.9211

Table 2: Continuous adsorption at Q= 5 ml/min and height= 1 cm

Time (min)	Ce. Concentration (ppm)			Ce/Co (50)	Ce/Co (100)	Ce/Co (150)
	50	**100**	**150**			
1	0.44	1.03	3.22	0.0088	0.0103	0.0214667
5	0.645	1.89	13.71	0.0129	0.0189	0.0914
10	15.99	54.35	82.99	0.3198	0.5435	0.5532667
15	27.69	70.81	122.055	0.5538	0.7081	0.8137
30	30.68	87.83	139.67	0.6136	0.8783	0.9311333
45	40.33	94.51	142.99	0.8066	0.9451	0.9532667
90	44.05	97.33	147.46	0.881	0.9733	0.9830667
180	46.66	98.8	148.92	0.9332	0.988	0.9928
270	46.37	99.21	149.74	0.9274	0.9921	0.9982667

Table 3: Continuous adsorption at 1 cm height and 100 ppm of Cd(II)

Time (min)	Ce. Flowrate (ml/min)		Ce/Co	Ce/Co
	5	**10**		
1	1.03	1.87	0.0103	0.0187
5	1.89	7.31	0.0189	0.0731
10	54.35	73.11	0.5435	0.7311
15	70.81	81.83	0.7081	0.8183
30	87.83	90.11	0.8783	0.9011
45	94.51	97.33	0.9451	0.9733
90	97.33	99.22	0.9733	0.9922
180	98.8	99.43	0.988	0.9943
270	99.21	99.82	0.9921	0.9982

شكر وتقدير

الحمد لله الذي وفقني ويسر لي أمري لإنجاز هذا البحث وله الشكر دائماً وأبدا.

الشكر والتقدير لأستاذي ومشرفي د. أسامة اكرم سعيد على توجيهاته وملاحظاته السديدة.

الشكر الوفير والدعاء بأن يبارك ويحفظ عائلتي (أمي وأبي وأخوتي) على كل ما قدموه لي من دعم في مسيرتي الدراسية.

لا أنسى ان اشكر ايضا كل من قدم لي المساعدة ويد العون.

الخلاصة

يعد تلوث المياه الناتج عن وجود المعادن الثقيلة مصدر قلق كبير استحوذ على اهتمام الباحثين بسبب آثاره الضارة على صحة الإنسان والبيئة. ومن المؤسف أن ما يقرب من 20 معدنًا، بما في ذلك الكادميوم، تقاوم عملية الإزالة أو التخفيض دون الخضوع للمعالجة الفيزيائية أو البيولوجية. واستجابة لهذا التحدي، برزت تقنية الامتزاز كوسيلة واعدة لاستخراج المعادن الثقيلة من المياه الملوثة. ضمن هذا البحث المحدد، تم تصنيع اثنين من المركبات النانوية المغناطيسية، P1 وP2 باستخدام طرق الترسيب المشترك. تم وصف مركبتي المحفز باستخدام XRD، وFE-SEM، وEDX، وFTIR، وAFM، وTEM، وBET، وتم استخدامهما بدقة لفحص السمات الهيكلية والمورفولوجية لهذه البوليمرات. كشف تحليل التوصيف عن التكوين الناجح للبنية النانوية البلورية، مما يؤكد التكامل الكيميائي للبوليمرات المشتركة في الجسيمات النانوية ذات القشرة الأساسية للسيليكات المغناطيسية. بالنسبة لكل من P1 وP2، تم تحديد متوسط الأحجام ليكون 29.13 نانومتر و14.66 نانومتر، على التوالي. علاوة على ذلك، أشارت قياسات مساحة السطح إلى قيم 37.7 متر مربع/جم لـ P1 و51.3 متر مربع/جم لـ P2. تسلط هذه النتائج الضوء على التوليف المتحكم فيه والخصائص المميزة للمواد المطورة.

تم فحص عملية الامتزاز الدفعي بشكل شامل، والتي تشمل أربعة متغيرات مستقلة: المدة التي تمتد من 5 إلى 405 دقيقة، ودرجة الحموضة للمحلول تتراوح من 2.5 إلى 12، وكتلة المحفز تتراوح بين 0.05 إلى 0.3 جم، وتركيز أيون الكادميوم (II) الممتد من 25 إلى 150 جزء في المليون عند درجة الحرارة المحيطة. حددت النتائج التجريبية الظروف المثالية لإزالة الكادميوم بشكل فعال عبر عملية الامتزاز باستخدام P1 وP2 كمواد ماصة: درجة حموضة محايدة، كتلة ماصة 0.3 جرام، وقت تلامس 405 دقيقة، وتركيز أولي لأيون الكادميوم (II) قدره 25 ملجم/لتر. أظهر العمود ذو القاعدة الثابتة على نطاق المختبر أن منحنيات الاختراق مستقلة عن معدل التدفق مما يحقق إزالة المعادن بنسبة 99٪ لمدة 405 دقيقة، عند درجة حموضة 8.0، وتركيز الأيونات المؤثرة 100 جزء في المليون، ومعدل تدفق 5 مل / دقيقة، وارتفاع السرير 1 سم. علاوة على ذلك، تم تسخير نماذج لانجميور وفروندليتش وتمكين ايزوثرم لفك وتوصيف عملية الامتزاز. كشفت النتائج أن نموذج فرندليتش أثبت أنه الأكثر ملاءمة لبيانات التوازن (R^2 = 0.98)، مما يشير إلى امتزاز غير مثالي ومتعدد الطبقات حيث ترتبط جزيئات ممتصة جديدة

بجزيئات ممتصة مسبقًا. على العكس من ذلك، التزم P2 بنموذج (0.96 = R^2) Langmuir، مما يشير إلى امتزاز أحادي الطبقة على سطح ممتز متجانس مع عدم وجود تفاعلات بين الجزيئات. في مجال الحركية، أظهرت الدراسة أن البيانات التجريبية لكل من المركبات النانوية تتوافق بشكل جيد مع نموذج الدرجة الثانية الزائفة مع معامل ارتباط مثالي تقريبًا يبلغ 0.99986 و 0.99989 على التوالي، متجاوزة النماذج الحركية الأخرى في الدقة.

وزارة التعليم العالي والبحث العلمي

جامعة النهـــــــرين/ كلية الهندســـة

تصنيع مركب الحديديك-بوليمر النانوي لإزالة الكادميوم من مياه الصرف الصحي

رسالة مقدمة

الى كليـــــة الهندســـــة في جامعة النهرين

وهي جزء من متطلبات نيل شهادة ماجستير/ علوم

في

الهندسة الكيمياوية

من قبل

زهراء عامر اسماعيل

(بكالوريوس في الهندسة الكيمياوية ٢٠٢٠ م)

بإشراف

أ.م.د. أسامة اكرم سعيد

جمادي الاول ١٤٤٥هـ

تشرين الثاني ٢٠٢٣مـ